Effect of particle size on LiNi0.6Mn0.2Co0.2O2 layered oxide performance in Li-Ion batteries

Adrien Soloy, Delphine Flahaut, Joachim Allouche, Dominique Foix, Germain Vallverdu, Emmanuelle Suard, Erwan Dumont, Lucille Gal, François Weill, Laurence Croguennec

Effect of particle size on $LiNi_{0.6}Mn_{0.2}Co_{0.2}O_2$ layered oxide performance in Li-ion batteries

Adrien Soloy[1], Delphine Flahaut[2,5], Joachim Allouche[2,5], Dominique Foix[2,5], Germain Salvato Vallverdu[2,5], Emmanuelle Suard[3], Erwan Dumont[4], Lucille Gal[4], François Weill[1,5,6] and Laurence Croguennec[1,5,6,]*

[1] Univ. Bordeaux, CNRS, Bordeaux INP, ICMCB UMR 5026, F-33600 Pessac, France

[2] Université de Pau et des Pays de l'Adour, E2S UPPA, CNRS, IPREM UMR 5254, 64000 Pau, France

[3] Institut Laue-Langevin, 71 avenue des Martyrs, 38042 Grenoble, France

[4] SAFT, Direction de la Recherche, 33074 Bordeaux, France

[5] RS2E, Réseau Français sur le Stockage Electrochimique de l'Energie, FR CNRS 3459, F-80039 Amiens Cedex 1, France

[6] ALISTORE-ERI European Research Institute, FR CNRS 3104, F-80039 Amiens Cedex 1, France

KEYWORDS: Li-ion battery, Layered oxide, NMC, morphology, reactivity, performances

ABSTRACT

The layered oxide $LiNi_{0.6}Mn_{0.2}Co_{0.2}O_2$ is a very attractive positive electrode material, as shown by good reversible capacity, chemical stability and cyclability upon long range cycling in Li-ion batteries and, hopefully, in a near future, in all-solid-state batteries. A large panel of synthesis conditions were explored in order to tailor the size of the primary particles for powders showing structures close to the ideal 2D layered structure (i.e. with less than 3.8% Ni^{2+} ions in the Li^+ sites). Materials with primary particle sizes ranging from 170 nm to 2 μm were obtained. Their electrochemical performance in Li-ion batteries and surface reactivity were characterized in different cycling conditions, as a function of the primary particle size. A significant impact on the performance and reactivity was observed, with obvious better reversible capacity and cyclability for the materials with primary particles ranging between 200 and 400 nm. The analysis of the solid electrolyte interphase formed at the interface between the positive electrode and the electrolyte has shown that larger particles had a larger proportion of lithium salt degradation products, induced by the larger amount of Li_2CO_3 at their surface. It was also shown that the degradation of the lithium salt was favoured at higher cycling rate, whereas that of the organic solvents is a little more favoured in larger potential windows with a higher cut-off voltage.

INTRODUCTION

The rapid development of the electric and hybrid vehicles industry is increasing the demand for Li-ion batteries with high energy densities and low cost. The best candidates at their positive electrodes are layered oxides $LiMO_2$ (M= Ni, Mn, Co).[1] Among all the possible compositions, the layered oxide $LiNi_{0.6}Mn_{0.2}Co_{0.2}O_2$ (NMC622) was shown to be one of the best compromise to combine the beneficial effects of Ni, Mn and Co for achieving good energy density together with structural and thermal stability as well as good cyclability.[1] Indeed, NMC materials with higher Ni contents show higher reversible capacities up to 200 mAh/g for $LiNi_{0.8}Mn_{0.1}Co_{0.1}O_2$ (NMC811),[2,3] but also higher volume expansion[1] and higher instabilities in the charged state due to the presence of a large amount of Ni^{4+} ions[3]. Inversely, at lower Ni contents, lower reversible capacities are obtained (for instance, 150 mAh/g for $LiNi_{1/3}Mn_{1/3}Co_{1/3}O_2$ (NMC111)[4]). In the meantime, as the Co and Mn contents increase, the proportion of Ni^{2+} increases versus that of Ni^{3+} in the pristine material, leading thus to a lower amount of unstable Ni^{4+} ions in the charge state of the battery and to higher cyclability and thermal stability.[3–5] Many efforts have been made in the past twenty years to control the synthesis and properties of these materials.[6–16] In order to optimize their electrochemical properties, different studies have been also focused on preparing them with different morphologies (i.e. particle size or shape).[9–11,13,17–19] Among many others, these layered oxides can be found in two well-known morphologies: the polycrystalline morphology with primary particles of several tens of nanometres organized in spherical aggregates[6,13] and the single-crystal morphology with primary particles of several micrometres.[11,13] The polycrystalline morphology is the most studied and reported in the literature.[6,8,12,13,20,21] However, it was shown that polycrystalline materials undergo anisotropic volume variations during cycling at the particle level, resulting in cracks within the spherical

agglomerates that modify the grain boundaries and disconnect the primary particles between them. This leads to continuous formation of Solid Electrolyte Interphase (SEI) due to the formation of fresh surfaces and to loss of cyclability and performance at high rates, especially when cycled in temperature.[22,23] Compared to the polycrystalline morphology, the single-crystal morphology enables to limit the risk of thermal runaway by decreasing the amount of heat released during the NMC thermal decomposition.[22] It was also shown that single-crystal particles had better performances at high rates at 45°C compared to polycrystalline particles, which performances are mainly affected by their large secondary particles and their larger charge-transfer resistance due to the grain boundaries between the primary particles.[22] However, despite that single-crystal particles show better cyclability than polycrystalline particles when cycled at 45°C, smaller first discharge capacity and higher irreversible capacity (IRC) are obtained when cycled at 30 and 45°C.[21,22,24]

To get a better insight into the relationship between the powder morphology, electrochemical performance and reactivity versus the organic liquid electrolyte, we managed to obtain NMC622 samples with precisely controlled stoichiometry and 2D structure and with various primary particle sizes. From a complete characterisation of these samples, it will be shown the optimum particle size depends on the choice of the electrochemical cycling conditions.

EXPERIMENTAL SECTION

$Ni_{0.6}Mn_{0.2}Co_{0.2}(OH)_2$ hydroxide was made by coprecipitation using similar synthesis protocol to that described by Pajot et al.[25] $NiSO_4.6H_2O$, $MnSO_4.H_2O$ and $CoSO_4.7H_2O$ (Sigma-Aldrich, ≥99%) were used as precursors to prepare an aqueous mixed solution of $NiSO_4.6H_2O$, $MnSO_4.H_2O$ and $CoSO_4.7H_2O$ (0.6:0.2:0.2 in molar ratio) with a total transition metal (TM) ion

concentration of 2 mol/L. This solution was pumped slowly into a continuously stirred tank reactor (CSTR). At the same time, a 4 mol/L aqueous solution of NaOH (Sigma-Aldrich, ≥99%), used as precipitant, and a NH_3 (Sigma-Aldrich, 28-30%) aqueous solution used as chelating agent, were separately fed into the reactor in order to maintain the pH value at 11 to avoid the formation of oxy-hydroxides. The CSTR was maintained at 60°C and under stirring at 300 rpm during the overall reaction and the final suspension was aged for 7 hrs. Afterwards, the mixed transition metal hydroxide is washed several times by centrifugation, with hot water to remove residual sodium and sulfate species until the pH of the solution becomes neutral. The hydroxide is then recovered by filtration and dried in an oven at 80°C overnight. To synthesize $Li(Ni_{0.6}Mn_{0.2}Co_{0.2})O_2$ layered oxides, the hydroxide is intimately mixed with lithium carbonate Li_2CO_3 (Sigma-Aldrich, ≥99%). A thermal treatment is performed at high temperature, between 780 and 930°C, with different Li_2CO_3 excesses (1 or 5 wt.% vs. the Li/TM ratio of 1.05) and under air or O_2 flow. This slight overlithiation (i.e. Li/TM ≥ 1.05) is required to obtain a layered structure with the smallest amount of Ni^{2+} ions in the Li sites. The samples are named according to the synthesis conditions used for their preparation: lithiation temperature (°C) - weight percentage of Li_2CO_3 excess - atmosphere.

The cationic composition of the lithiated layered oxides was determined by Inductively Coupled Plasma - Optical Emission Spectrometry (ICP-OES) (Varian ICP/OES 720 ES) after their complete dissolution into a mixture of hydrochloric acid and nitric acid (HCl/HNO_3: 2/1 in volume ratio). Each sample was dissolved twice and each solution is measured 5 times, meaning the ICP values given hereafter are averages of 10 measurements. The carbon content of the powders was also determined using a CHNS elemental Thermo Fischer Scientific analyser equipped with an automatic sampler. Powder X-Ray diffraction (XRD) patterns were recorded

using a PANalytical X'Pert MPD Pro diffractometer equipped with a Cu radiation X-ray tube, to determine the purity and structure of the synthesized materials. The XRD patterns were collected in the angular range of 10-80°(2θ) with 0.008° intervals, for a total acquisition time of around 35 hrs. Neutron Powder Diffraction (NPD) was performed using the high-resolution powder diffractometer D2B at Institut Laue Langevin (ILL, Grenoble, France). The samples were contained in a vanadium tube with a diameter of 8 mm. The NPD patterns were collected at room temperature with a wavelength $\lambda = 1.5947(1)$ Å, in the angular range of 0-160°(2θ) with 0.05° intervals for a total acquisition time of around 5 hrs. The collected XRD and NPD patterns were refined by the Rietveld method using FullProf software.[26] The peaks profiles were described by a Pseudo-Voigt function, and the full width at half maximum by a Caglioti function. For the NPD patterns, due to the geometry of the diffractometer (transmission mode), a correction factor μR of 0.79 was applied to take into account the absorption of the signal by the powder and thus the decrease of diffracted intensities.[27] The particles morphology and size were observed by scanning electron microscopy (JEOL 6700F & Hitachi S4500 FEG), after being metallized by gold deposition. Average primary particle sizes were determined by measuring 100 particles using the software ImageJ. Granulometry measurements were performed using a Malvern Mastersizer 2000. The powders were previously dispersed in distilled water and sonicated for 1 min. Each sample was measured 3 times with 10 seconds apart. The results given in that paper are thus an average of those 3 measurements. BET surface areas were determined using a Micromeritics 3FLEX analyser. The powders were previously degassed under vacuum at 90°C for 1 hr and then at 150°C for 10 hrs.

The surface composition of the pristine powders, pristine electrodes and corresponding cycled electrodes was determined by X-ray Photoelectron Spectroscopy (XPS) using an ESCALAB 250

Xi spectrometer and a Kratos Axis Ultra DLD spectrometer with a monochromatized Al-Kα X-Ray source (hν = 1486.6 eV). In both cases, a neutraliser gun was used to minimize surface charging. For the pristine powders, the spectral calibration was carried out using the C-C/C-H component (285 eV) originated from the usual surface carbon contamination in C1s core peaks. For the pristine and cycled electrodes, it was carried out using the CF_2 component (291 eV) originated from the PVDF polymeric binder in C1s core peaks. The peak fitting process was carried out using a non-linear Shirley-type background. The peak positions and areas were optimized by weighted least-squares calculation method using 70% Gaussian and 30% Lorentzian line shapes. The quantification of surface composition was performed using basis of Scofield's relative sensitivity factors corrected by specific values depending on the apparatus.[28] The quantification and spectra fitting were carried out using CASA XPS software.

The samples were electrochemically tested in CR2032-type coin cells consisting of a positive electrode and a lithium foil as negative electrode, separated by 2 Celgard 2400 separators. The positive electrodes were prepared by coating a slurry on an aluminium foil as current collector. The slurry was prepared by mixing the active material with the carbon black and the polyvinylidene fluoride (PVDF, Sigma, average Mw ≈ 534000 g/mol by Gel Permeation Chromatography (GPC)) binder (92:4:4 wt.%) in N-methyl-2-pyrrolidone (NMP) (Sigma Aldrich, 99%). The electrolyte was 1 mol/L $LiPF_6$ dissolved in a mixture of dimethyl carbonate (DMC) and fluoro ethylene carbonate (FEC) in a 70/30 volume ratio. The coin cells were assembled in an argon-filled glovebox and were cycled using a VMP (Biologic) in galvanostatic mode. Galvanostatic Intermittent Titration Technique (GITT) experiments were performed at a constant current pulse of C/100 for 30 min and then rest for 15 hrs to stabilize the cell voltage between 2.5 and 4.6V. The electrodes were recovered after cycling for analyses. Coin cells were

dismantled after cycling in an Ar-filled glovebox. Electrodes were washed 3 times with dimethyl carbonate (DMC) and dried under vacuum.

RESULTS AND DISCUSSION

Structural and physico-chemical characterizations

Starting from a mixed transition metal hydroxide precursor synthesized by coprecipitation (see Figure S1 given in supporting information for more information on its composition, structure and morphology), lithiations were performed in different conditions. First, lithiations were performed at different temperatures with a 5 wt.% excess of Li_2CO_3 under air in order to determine the impact of the thermal treatment temperature. Figure S2 depicts the XRD patterns for the corresponding samples. As expected from previous works,[10–13,29] the temperature has a significant impact on the structure of the NMC-type materials. The optimum temperature range, in which the structure is the closer to an ideal 2D packing, with very few divalent nickel ions in the lithium site, was found to be 810 - 930°C. Indeed, if all materials crystallize in an α-$NaFeO_2$-type layered structure described in the $R\bar{3}m$ space group, those obtained in that temperature range show XRD patterns with the more separated (018) and (110) diffraction lines, the higher (003)/(104) intensity ratios (> 1.2) (see Figure S2a) and the smaller lattice parameters (see Figure S2b) giving the higher c/a ratios (> 4.95) (see Figure S2c).[12,14,15,30] These factors allow to perform a first evaluation of how far from the ideal cationic distribution the structure of the synthesized sample is. Additional lithiations were performed with a lower amount of Li_2CO_3 excess (1 wt.%) and/or under O_2. Among all these materials, 11 were selected to be studied in more details. Their XRD patterns are given in Figure 1. The 11 samples can be sorted into 3

different series: the materials made with 5 wt.% excess of Li_2CO_3 in air ("5-air" samples), those made with 1 wt.% excess of Li_2CO_3 in air ("1-air" samples) and those made with 5 wt.% excess of Li_2CO_3 under O_2 flow ("5-O_2" samples). Tiny amounts of impurities were detected in the 5-air samples, as shown by the low intensity peaks in the 22-23° region in the inset. Those peaks were tentatively attributed to one Mn-rich and one Co-rich oxides but their identification remains uncertain because only the main peaks of their XRD patterns could be observed.

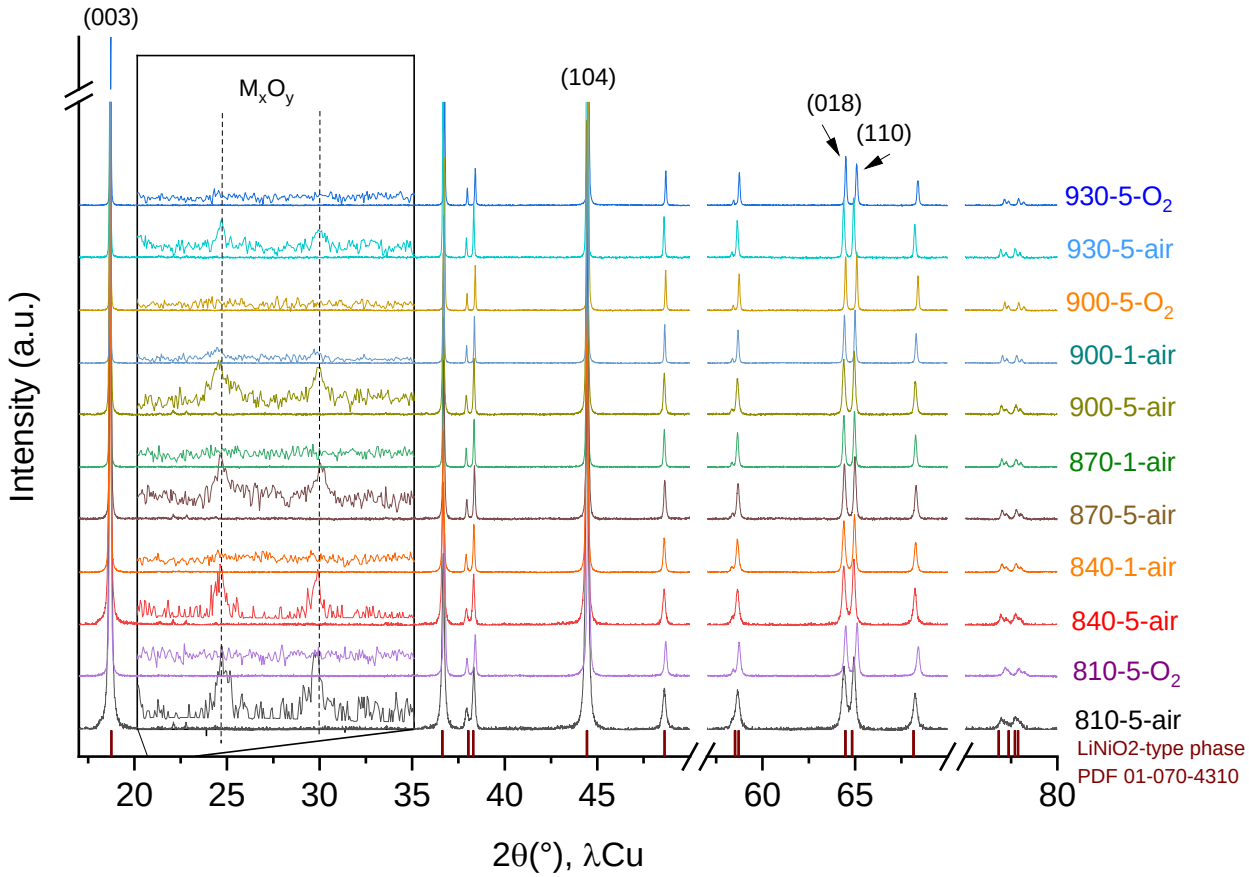

Figure 1. X-ray diffraction patterns obtained for the synthesized samples. The samples are named as follows: Lithiation temperature (°C) - excess of Li_2CO_3 (wt.%) - atmosphere. TM oxides M_xO_y were detected as impurities in very small amounts in the 5-air samples (in inset, the intensity is multiplied by a factor of ca. 10).

As shown by the chemical analyses gathered in Table S1, all the selected samples show compositions in transition metals close to the expected one, i.e. the stoichiometry Ni:Mn:Co of 6:2:2. A slight overlithiation is observed with Li/TM ratios larger than 1 for all the samples, with traces of carbon estimated by gas phase chromatography analyses to be smaller than 1 wt.%. This was attributed to the presence of Li_2CO_3 in the powders. This carbonate can be, either a residue of the Li precursor used in excess during the synthesis, or formed by reaction of the lithiated layered oxide with ambient air after the synthesis.[31–33]

Neutron diffraction measurements have been combined to XRD for the "5-air" series of samples to evaluate the possible presence of extra Ni^{2+} ions in the interslab spaces.[13,34–38] Indeed, NPD enables to localize the different transition metals present in the NMC layered structure due to the Fermi lengths different in magnitude and in sign for Li ($-0.19.10^{-12}$ cm), Ni ($1{,}03.10^{-12}$ cm), Mn ($-0.37.10^{-12}$ cm) and Co ($0.25.10^{-12}$ cm).[39–42] Figure 2 shows, as an example, the Rietveld refinement of the neutron and X-ray diffraction patterns recorded for the sample 810-5-air. The small residue observed between the calculated and the experimental patterns proves that the structure of this compound is well described in the $R\bar{3}m$ space group. The neutron diffraction patterns refinements confirm the presence of 3.5% extra Ni^{2+} ions in the interslab spaces and that the transition metals occupancies in the slab are very close to 6:2:2, confirming that the impurities detected in XRD are in very small amounts and do not affect significantly the composition of our layered phases. Details on the structural parameters of this sample can be found in Table S2.

The lattice parameters and the amount of extra Ni^{2+} ions in Li^{+} sites as determined for all samples are gathered in Table 1 and compared as a function of the synthesis conditions. These refinements confirm the structures of all the samples are close to the ideal 2D layered

one[12,14,15,30]. Thanks to the amounts of Ni^{2+} ions in Li sites determined from XRD patterns refinements, the cationic distribution is proposed for each sample, considering the charge balance and the stabilization of Ni in the divalent state in the interslab spaces and of Co and Mn in the trivalent and tetravalent states respectively in the slabs.[38]

Note that the materials synthesized under an O_2 flow have the most layered structures as less than 1.8% Ni^{2+} ions are present in Li^+ sites. On the contrary, the highest amount is observed for the samples obtained under air at 900°C and 930°C (i.e. 3.8% and 3.7% respectively) with 5% of Li_2CO_3. These results are in accordance with previous works, in which higher amounts of Ni^{2+} ions in Li^+ sites were obtained for syntheses carried out under air, and even more at higher synthesis temperatures (T > 900°C).[10,13]

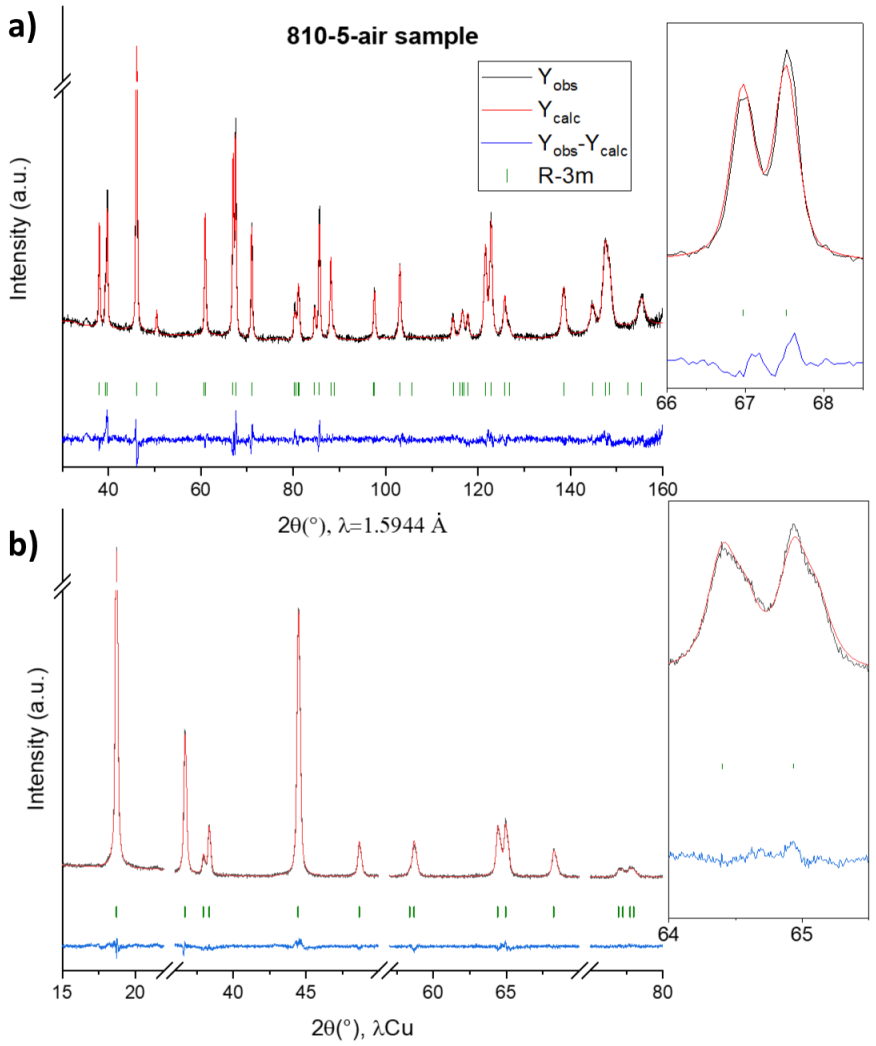

Figure 2. Refinements of the neutron (a) and X-ray (b) diffraction patterns recorded for the sample 810-5-air. Axis breaks were used in order highlight better the quality of the refinements, as shown also by the enlargements of the (018)/(110) diffraction lines given on the right of the figure.

Table 1. Comparison of the lattice parameters, c/a ratios, compositions and cation distributions calculated from the Rietveld refinements of the X-ray diffraction patterns. The Average primary particle sizes were determined by measuring 100 primary particles on SEM pictures with the software ImageJ. The corresponding SEM images are given in Figure 3, Figure 4 and Figure S3.

Samples	a (Å)	c (Å)	c/a	Composition and cation distribution	Average primary particle size
930-5-O$_2$	2.86356(3)	14.2006(4)	4.9591(2)	$(Li^{+}_{0.982(3)}Ni^{2+}_{0.018(3)})(Ni^{2+}_{0.222(4)}Ni^{3+}_{0.371(5)}Mn^{4+}_{0.204(1)}Co^{3+}_{0.204(1)})O_2$	2.1 µm

930-5-air	2.86988(3)	14.2189(5)	4.9545(2)	$(Li^{+}_{0.963(3)}Ni^{2+}_{0.037(3)})(Ni^{2+}_{0.244(4)}Ni^{3+}_{0.341(5)}Mn^{4+}_{0.207(1)}Co^{3+}_{0.207(1)})O_2$	1.2 µm
900-5-O_2	2.86298(3)	14.2021(3)	4.9606(2)	$(Li^{+}_{0.985(3)}Ni^{2+}_{0.015(3)})(Ni^{2+}_{0.218(4)}Ni^{3+}_{0.376(5)}Mn^{4+}_{0.203(1)}Co^{3+}_{0.203(1)})O_2$	810 nm
900-1-air	2.86691(3)	14.2144(3)	4.9581(2)	$(Li^{+}_{0.981(3)}Ni^{2+}_{0.019(3)})(Ni^{2+}_{0.223(4)}Ni^{3+}_{0.370(5)}Mn^{4+}_{0.204(1)}Co^{3+}_{0.204(1)})O_2$	1.1 µm
900-5-air	2.86846(3)	14.2196(5)	4.9572(2)	$(Li^{+}_{0.962(3)}Ni^{2+}_{0.038(3)})(Ni^{2+}_{0.246(4)}Ni^{3+}_{0.339(5)}Mn^{4+}_{0.208(1)}Co^{3+}_{0.208(1)})O_2$	400 nm
870-1-air	2.86789(3)	14.2190(4)	4.9580(2)	$(Li^{+}_{0.973(3)}Ni^{2+}_{0.027(3)})(Ni^{2+}_{0.232(4)}Ni^{3+}_{0.357(5)}Mn^{4+}_{0.205(1)}Co^{3+}_{0.205(1)})O_2$	370 nm
870-5-air	2.86778(6)	14.2160(5)	4.9571(3)	$(Li^{+}_{0.966(3)}Ni^{2+}_{0.034(3)})(Ni^{2+}_{0.241(4)}Ni^{3+}_{0.346(5)}Mn^{4+}_{0.207(1)}Co^{3+}_{0.207(1)})O_2$	280 nm
840-1-air	2.86755(6)	14.2169(5)	4.9579(3)	$(Li^{+}_{0.971(3)}Ni^{2+}_{0.029(3)})(Ni^{2+}_{0.235(4)}Ni^{3+}_{0.354(5)}Mn^{4+}_{0.206(1)}Co^{3+}_{0.206(1)})O_2$	240 nm
840-5-air	2.86920(6)	14.2147(8)	4.9542(4)	$(Li^{+}_{0.977(3)}Ni^{2+}_{0.023(3)})(Ni^{2+}_{0.228(4)}Ni^{3+}_{0.363(5)}Mn^{4+}_{0.205(1)}Co^{3+}_{0.205(1)})O_2$	200 nm
810-5-O_2	2.86252(6)	14.2014(6)	4.9612(3)	$(Li^{+}_{0.982(3)}Ni^{2+}_{0.018(3)})(Ni^{2+}_{0.222(4)}Ni^{3+}_{0.371(5)}Mn^{4+}_{0.204(1)}Co^{3+}_{0.204(1)})O_2$	240 nm
810-5-air	2.86952(9)	14.2152(9)	4.9539(5)	$(Li^{+}_{0.965(3)}Ni^{2+}_{0.035(3)})(Ni^{2+}_{0.242(4)}Ni^{3+}_{0.344(5)}Mn^{4+}_{0.207(1)}Co^{3+}_{0.207(1)})O_2$	170 nm

Figure 3 compares the morphologies of four of the "5-air" samples, the 810-5-air, 870-5-air, 900-5-air and 930-5-air samples, by SEM. The average primary particle size increases with the lithiation temperature, from 170 nm in diameter at 810°C to 1.2 µm at 930°C as detailed in Table 1. To estimate the variation of specific surface area generated by this variation of primary particle size, surface area measurements were carried out on the "5-O_2" samples as they are representative of the particle size range observed for those samples, from 200 nm to 2 µm. The results are shown in Table S3, the specific surface area decreases from around 3 m²/g for the 240 nm particles of the 810-5-O_2 sample to around 1 m²/g for the 2.1 µm particles of the 930-5-O_2 sample. Despite being very low and at the limit of accuracy of the technique, this evolution is in good agreement with an expected decrease of the surface area for larger particles. The pore volumes are also indicated and they show that the 810-5-O_2 sample with 240 nm particles is more porous than the 930-5-O_2 sample with 2.1 µm particles. The three samples synthesized at 900°C, as well as the corresponding distribution in sizes, are compared in Figure 4: larger primary particles are obtained under O_2 in comparison to those obtained under air for 5% of Li_2CO_3. Similarly, the smaller excess of lithium carbonate used during the synthesis gives larger primary particles in the same atmosphere synthesis. The 900-5-air sample has thus a narrow

distribution of smaller primary particle size compared to the two others. The morphology of the other samples is shown in Figure S3. For all the materials, the primary particles are embedded into large, non-spherical and porous agglomerates. To go further in the study of the morphology of the materials, laser granulometry measurements were performed. Figure S4 shows very similar particles' size distributions, in volume or in number percentages, for the three samples synthesized at 900°C with or without applying 1 min sonication. The appearance of a group of smaller particles on the sizes distribution in volume percentage (Figure S4b) as well as the shift of the distribution in number percentage towards smaller sizes after sonication (Figure S4d) reflect the deagglomeration of some particles and confirm that the primary particles are embedded into large micrometric agglomerates. As shown by the particles' size distribution in number percentages given in Figure S4, the average primary particle sizes are in good agreement with the ones determined by the SEM pictures analysis, confirming also that the smaller primary particles are obtained for the 900-5-air sample. The distribution in size expands from 0.1 to 1.0 μm for the primary particles observed by SEM, and from 0.1 to 3.0 μm for the primary particles and aggregates observed by laser granulometry.

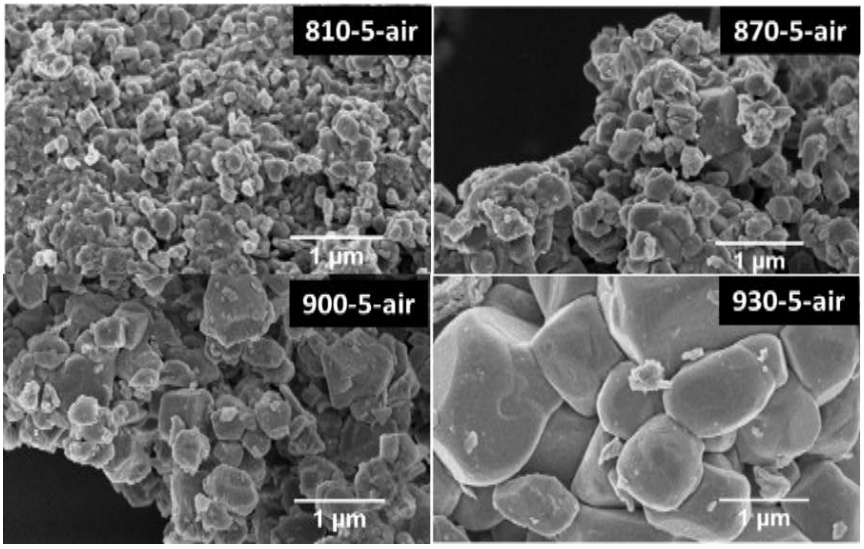

Figure 3. Morphologies obtained for the 810-5-air, 870-5-air, 900-5-air and 930-5-air samples, selected in the "5-air" series.

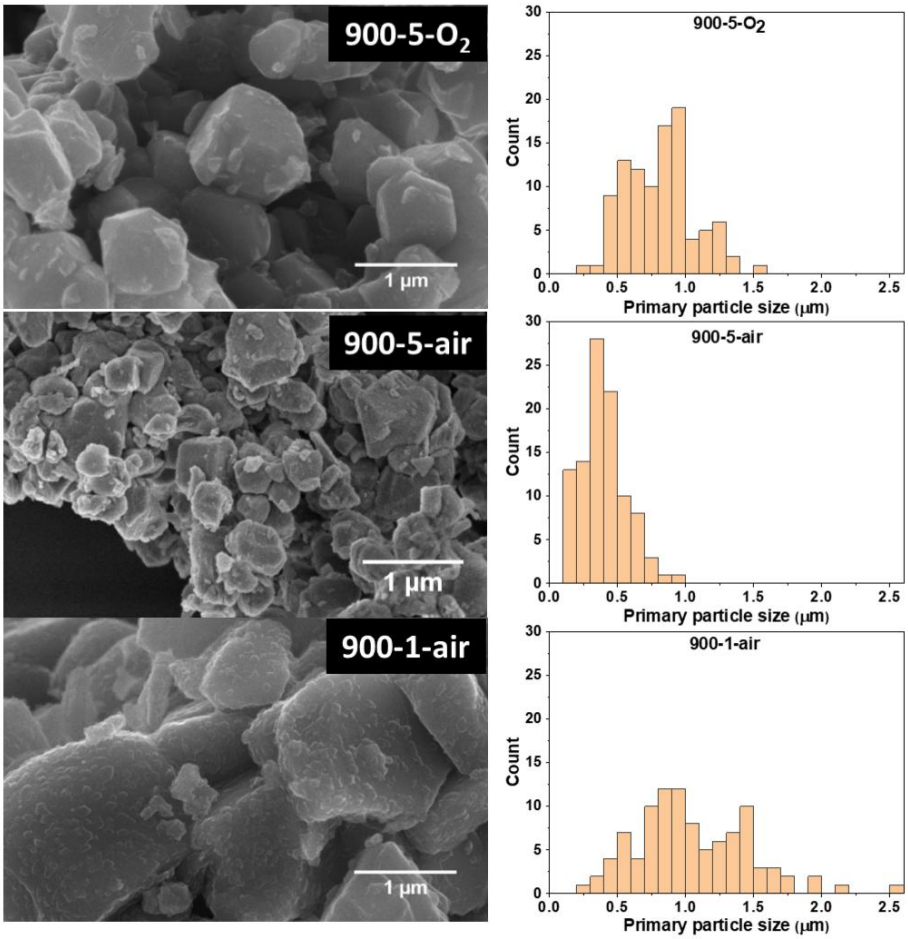

Figure 4. Morphologies of the samples synthesized at 900°C and the corresponding size distributions determined by Image J considering 100 particles.

Surface analyses

The surface of these samples was analysed by XPS. Figure 5 compares as an example the C1s, O1s and Li1s spectra obtained for the samples synthesized at 900°C.

The C1s spectra are decomposed into four contributions observed at 285.0, 286.4, 288.6 and 290.1 eV and corresponding to C-C/C-H, C-O, C=O/O-C=O and CO_3^{2-} environments respectively.[43,44] The O1s spectra exhibit a component at 529.7 eV corresponding to O^{2-} anions in the NMC crystalline network and two other components located at higher binding energies assigned CO_3^{2-}/O-C=O/C=O and C-O environments. In the 45-80 eV binding energy range, Ni3p, Co3p, Li1s and Mn3p core peaks have been identified. On the basis of literature, the Ni3p

core peak at 68.1 eV corresponds to nickel in a mixed valence Ni^{2+}/Ni^{3+}, the Co3p core peak at 61.3 eV corresponds to Co^{3+} and the Mn3p core peak at 50.0 eV corresponds to Mn^{4+} in an oxygen environment.[45,46] Those peaks were chosen to perform a more precise quantitative analysis as they are in the same binding energy range as opposed to the corresponding 2p core peaks. The Li1s peak is decomposed into two components at 54.4 eV and 55.6 eV attributed respectively to Li atoms in the NMC crystalline network (labelled Li_{NMC}) and Li_2CO_3 (labelled Li_2CO_3).

First, we can easily observe that, under air atmosphere, limited use of Li_2CO_3 excess increases the proportion of the O_{NMC} contribution to the O1s core peak. The same observation can be made when the synthesis atmosphere is changed from air to O_2 for a given Li_2CO_3 content. This observation is confirmed by the decrease of the components located at 290.0 eV in the C1s spectra and at 55.6 eV in the Li1s spectra, associated both to carbonate species, when the Li_2CO_3 excess is lowered or when the synthesis atmosphere is O_2. The less covered particles by adsorbed species and/or carbonate species are obtained for the 900-1-air and 900-5-O_2 samples.

The complete quantitative analysis of the 900-5-air material is shown in Table S4 as an example. The chemical surface analyses of the three samples, displayed in atomic percentages, are summarized in Table 2 and in Table 3. Only the most interesting values obtained from those quantitative analyses are shown hereafter. In Table 2, the atomic percentages of the Li_2CO_3 contributions in the Li1s and C1s spectra, extracted from global quantification, are given, with the contribution attributed to the oxygen atoms in the NMC network (O_{NMC}) with respect to the rest of the O1s spectra. Thus, we can confirm that the samples 900-1-air and 900-5-O_2 are those showing the lowest carbonate concentrations on their surface, and thus the highest concentrations of transition metals and oxygen assigned to the layered material. The results in Table 3 (resp.

Table S5) give the transition metal stoichiometry on extreme surface for the materials synthesized at 900°C (resp. all samples) which is closed to 6:2:2, as reported for ICP measurements, showing that the composition does not differ much from the surface to the bulk. Moreover, for a given atmosphere, the %.at range value of carbonate species at the surface (see Table S6) is directly related to the amount of Li excess during synthesis. For each series of materials (same Li_2CO_3 and atmosphere conditions), the trends is that a higher proportion of Li_2CO_3 is detected as the synthesis temperature is increasing which could be related to the particle size increase. This remaining Li_2CO_3 is prone to be found at the extreme surface as no impurities associated to carbonate species have been identified by XRD measurements and very small amount (<1 wt.%) of carbon were detected in the bulk by gas phase chromatography.

Note that there is no relationship between the quantity of Li_2CO_3 measured at the surface and the amount of Ni^{2+} ions in the interslab spaces as determined by the Rietveld refinement. Indeed, the "5-O_2" samples have very similar amounts of Ni^{2+} ions in the interslab spaces (between 1.5 and 1.8%, as shown in Table 1) but different amounts of Li_2CO_3 at their surface.

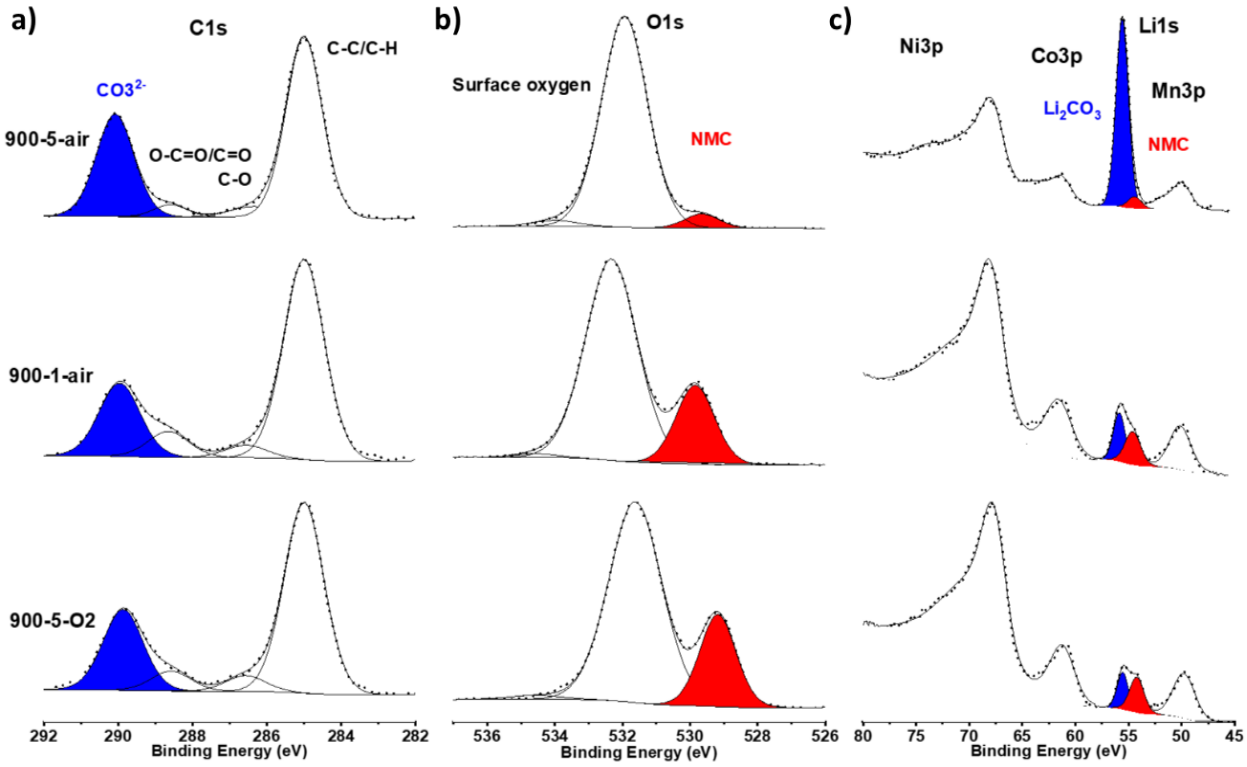

Figure 5. C1s (a), O1s (b) and Li1s (c) XPS spectra of the samples synthesized at 900°C. The C_{CO_3} and $Li_{Li_2CO_3}$ peaks are highlighted in blue and the O_{NMC} and Li_{NMC} peaks are highlighted in red. The dots represent the experimental data and the lines the fitted spectra.

Table 2. Comparison of the contribution of the carbonates species in the C1s and Li1s spectra, and the contribution of oxygen from the electrode material in atomic percentages extracted from the global quantitative analyses performed from XPS spectra of the materials synthesized at 900°C.

	Atomic percentages		
Samples	**C1s (Li_2CO_3)**	**Li1s (Li_2CO_3)**	**% O_{NMC} in O1s**
900-5-O_2	6.3	12.7	23.5
900-1-air	6.2	13.6	22.4
900-5-air	10.0	30.4	4.7

Table 3. Transition metal ratio of the materials synthesized at 900°C obtained from Ni, Mn and Co atomic percentages extracted from the global quantitative analyses performed from XPS spectra.

	Atomic percentages				
Samples	**Ni 3p**	**Mn 3p**	**Co 3p**	**ΣTM**	**(Ni:Mn:Co)/ΣTM**
900-5-O_2	5.8	1.3	1.4	8.5	0.68 : 0.15 : 0.16
900-1-air	4.9	1.1	1.2	7.2	0.68 : 0.15 : 0.17
900-5-air	1.6	0.4	0.4	2.4	0.67 : 0.17 : 0.17

Electrochemical analyses

These samples were electrochemically tested in CR2032 type coin cells versus Li in galvanostatic mode. Figure 6 compares the results obtained for the "5-air" materials (Figure 6a), the "5-O_2" materials (Figure 6b) and the samples synthesized at 900°C (Figure 6c). They were cycled at C/20 (1 charge-discharge cycle in 20 hours) in the 2.5-4.3V potential range. The 1st discharge capacities, irreversible capacity rates (IRCs) and capacity retention after 30 cycles are gathered for comparison in Table 4.

The materials "5-air" deliver a 1st discharge capacity between 149 and 165 mAh/g with an irreversible capacity (IRC) between 11 and 21% (Figure 6a and in Table 4). The samples with the largest primary particles, 400 nm and 1.2 µm, show the highest 1st discharge capacities of 165 mAh/g and the lowest IRCs of 11-13%. In inset of figure 6a, the corresponding derivative curves dQ/dV are compared. They are very similar for all samples. Only the material with 170 nm primary particles shows a slightly larger polarization. Indeed, the corresponding oxidation and reduction peaks are located at 3.79 V and 3.72 V, while they are at 3.76 V and 3.73 V respectively for the other samples. Figure S5 shows the evolution of the discharge capacity

delivered by those samples as a function of the number of cycles. The materials 870-5-air and 900-5-air with primary particles of around 280 and 400 nm respectively deliver higher capacities. Moreover, the sample 810-5-air with 170 nm primary particles shows a better capacity retention (95% after 30 cycles, see Table 4).

All samples of the "5-O_2" series have very similar performances as shown in Table 4 and Figure 6b, with 1st discharge capacities between 159 and 173 mAh/g and IRCs between 7 and 11%. The sample 810-5-O_2 with 240 nm primary particles has a 1st discharge capacity of 173 mAh/g, similar to that of the sample 900-5-O_2 with 810 nm primary particles (170 mAh/g) and much higher than that of the sample 930-5-O_2 (159 mAh/g) with primary particles of 2.1 µm. Larger discharge capacities are reached compared to the previous series of materials, probably in relation with the smaller amounts of Ni^{2+} in Li^{+} sites for these materials. As shown in inset of Figure 6b, very similar polarization curves are observed for the "5-O_2" samples during the 1st cycle. Figure S6 shows that the materials 810-5-O_2 and 900-5-O_2 with 240 nm and 810 nm primary particles deliver larger specific capacities and capacity retentions. Inversely, the sample 930-5-O_2 with 2.1 µm primary particles delivers significantly lower capacities with a lower capacity retention of 82% after 30 cycles versus 94% and 92% for the 810-5-O_2 and 900-5-O_2 samples respectively (Table 4).

The materials synthesized at 900°C deliver a 1st discharge capacity ranging between 165 and 176 mAh/g with IRCs between 8 and 11% (Table 4 and Figure 6c). From the evolution of the discharge capacities delivered by those three samples, it can be observed that the 900-1-air sample shows the highest 1st discharge capacity of 176 mAh/g while the 900-5-O_2 shows the best capacity retention of 92% after 30 cycles (see Table 4 and Figure S7), both showing the smallest

amounts of Ni^{2+} ions in Li^{+} sites (3.8% for 900-5-air versus 1.5% for 900-5-O_2 and 1.9% for 900-1-air).

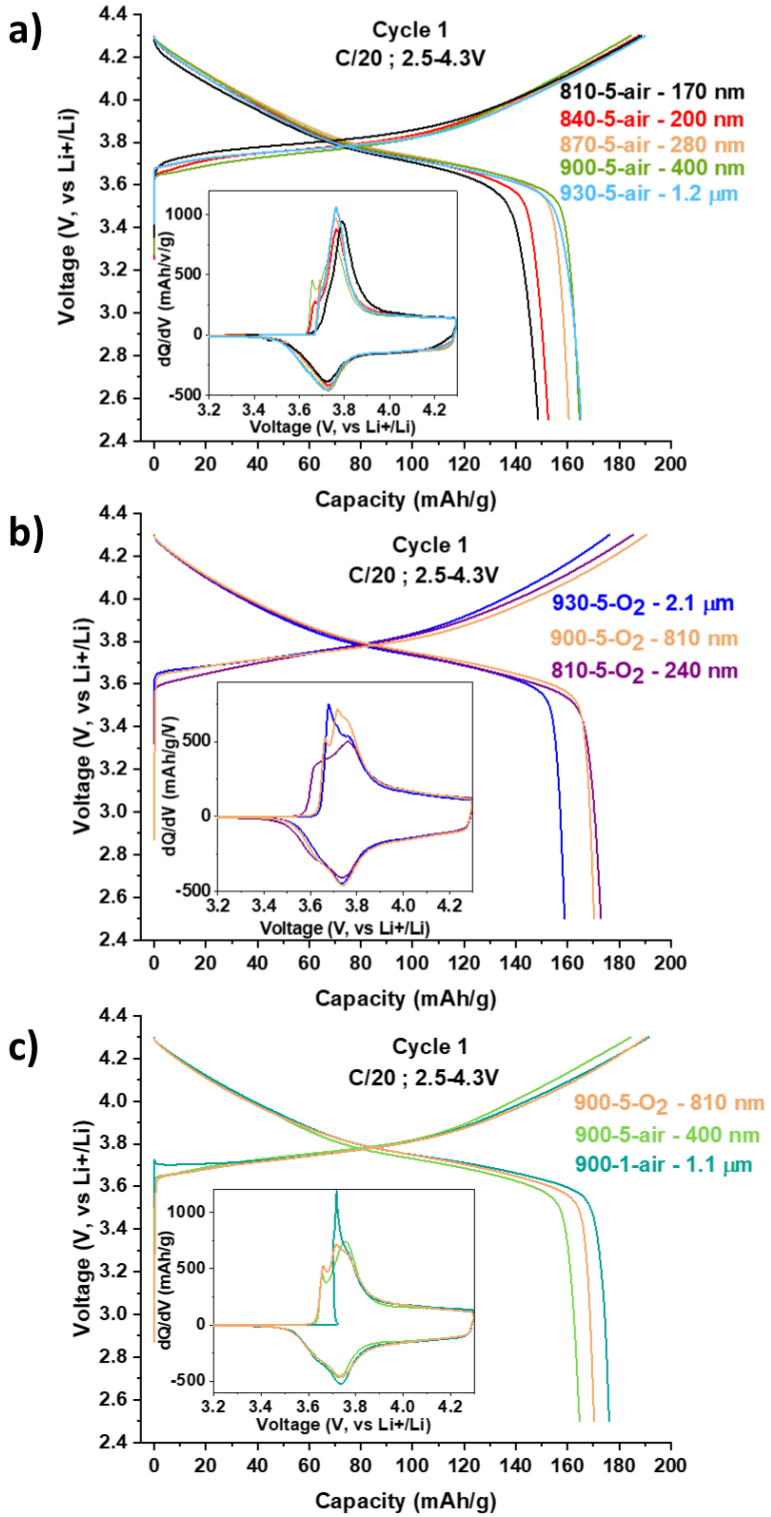

Figure 6. Charge-discharge curves and corresponding dQ/dV curves obtained at 1st cycle for the "5-air" samples (a), the "5-O_2" samples (b) and the samples synthesized at 900°C (c).

Table 4. 1st discharge capacities, irreversible capacities rates (IRC, %) and capacity retentions determined for the "5-air" samples, "5-O_2" samples and the samples synthesized at 900°C.

			C/20 ; 2.5-4.3V		
Samples	**%Ni_{Li}**	**Average primary particle size**	**1st discharge capacity (mAh/g)**	**IRC (%)**	**Capacity retention after 30 cycles (%)**
810-5-air	3.5	170 nm	149	21	95
840-5-air	2.3	200 nm	152	19	87
870-5-air	3.4	280 nm	160	15	93
900-5-air	3.8	400 nm	165	11	88
930-5-air	3.7	1.2 µm	165	13	61
810-5-O_2	1.8	240 nm	173	7	94
900-5-O_2	1.5	810 nm	170	11	92
930-5-O_2	1.8	2.1 µm	159	10	82
900-1-air	1.9	1.1 µm	176	8	82

To investigate further the influence of the primary particle size on the electrochemical performances of these NMC622 materials, four of the "5-air" samples were cycled in harder conditions: (i) at higher rate C/5 (vs. C/20 as just discussed) and (ii) in a larger potential window 2.5 - 4.6 V (vs. 2.5 - 4.3 V previously). The 810-5-air, 840-5-air, 900-5-air and 930-5-air samples were chosen to be compared as they allow to scan the particle size range studied in our reference "5-air" series of materials. As shown by the comparison between Figure 7a and Figure 7b, a higher cycling rate leads to lower performances whatever the particle size. The largest performance drops are observed for samples with either the largest (930-5-air sample) or the smallest particles (810-5-air sample) (Table 5). As shown in Figure S8, the 400 nm particles (900-5-air) offer the best performances with significantly larger capacities compared to the three other samples and good capacity retention. When the samples are cycled at the same cycling rate (C/5) but in larger potential window with a cut-off voltage of 4.6V (Figure 7c), as expected, larger reversible capacities are obtained whatever the particle size, as a larger amount of Li^+ ions are deintercalated from the layered structure. As for the two previous cycling conditions, the best

performances at 1st cycle are obtained for the 400 nm particles (900-5-air sample) with a 1st discharge capacity of 185 mAh/g and an irreversible capacity rate of 16% (Table 5). However, as shown in Figure S9, those particles have a declining capacity retention compared to the previous cycling conditions and the best capacities are obtained for the 200 nm particles (840-5-air sample) after 5 activation cycles.

Table 5. 1st discharge capacities and irreversible capacities (IRC, %) of four samples representative of the "5-air" series cycled in different conditions

	C/20 ; 2.5-4.3V		**C/5 ; 2.5-4.3V**		**C/5 ; 2.5-4.6V**	
Sample	**1st discharge capacity (mAh/g)**	**IRC (%)**	**1st discharge capacity (mAh/g)**	**IRC (%)**	**1st discharge capacity (mAh/g)**	**IRC (%)**
810-5-air (170 nm)	149	21	119	34	151	30
840-5-air (200 nm)	152	19	128	27	165	25
900-5-air (400 nm)	165	11	158	18	185	16
930-5-air (1.2 µm)	165	13	87	30	130	38

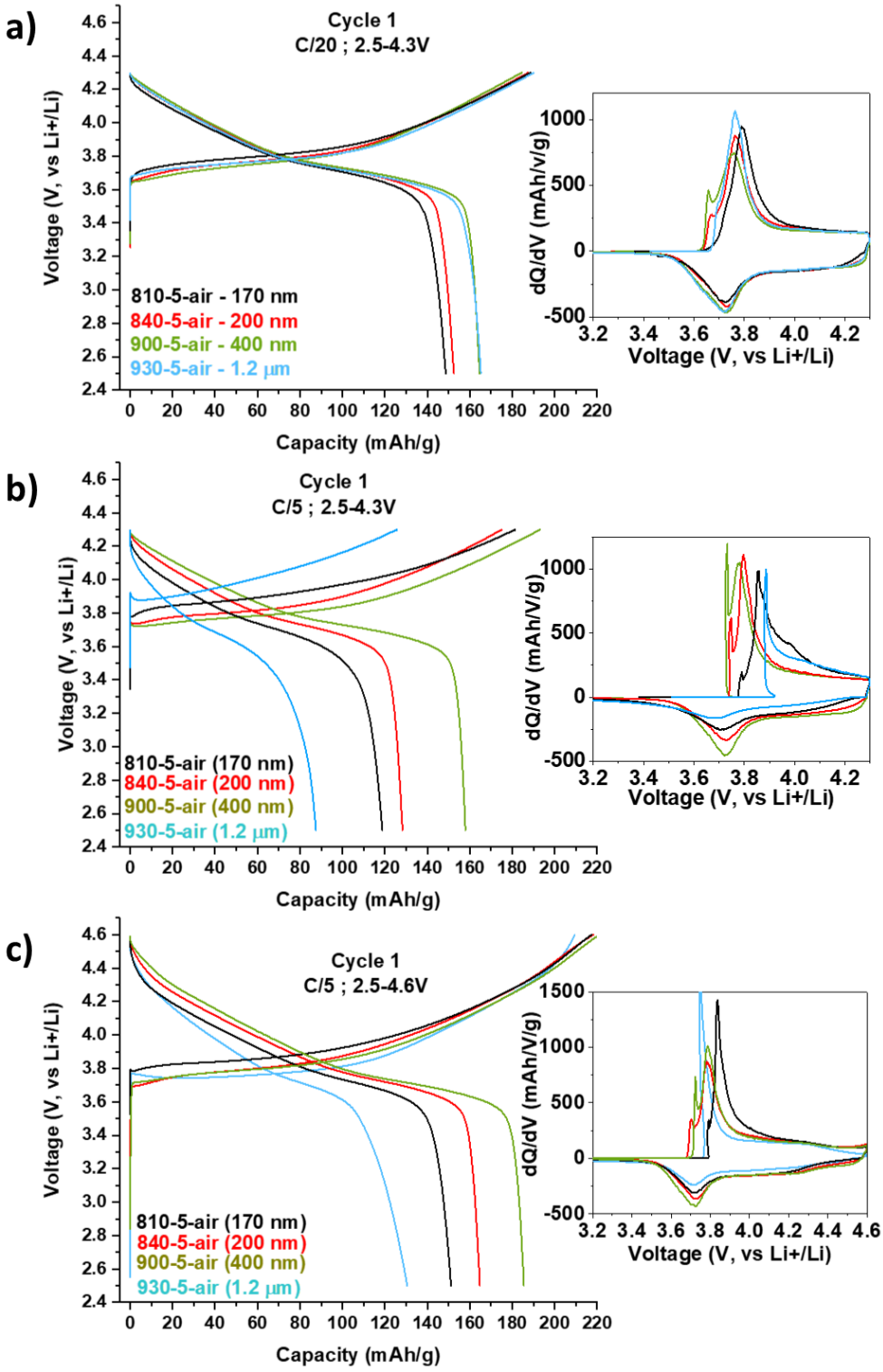

Figure 7. Charge-discharge curves and corresponding dQ/dV curves obtained for the 1st cycle at C/20 2.5-4.3V (a); C/5 2.5-4.3V (b) and C/5 2.5-4.6V (c) for four samples representative of the "5-air" series.

To better understand those differences of performances and investigate the impact of those different cycling conditions on the electrode/electrolyte interface composition, XPS analyses were performed on cycled electrodes.

Electrode/Electrolyte interface analysis

XPS analyses were performed on electrodes recovered after cycling of the 900-5-air sample (400 nm primary particles), the one that showed good electrochemical performances regardless of the cycling conditions. One electrode was analysed after cycling at C/20 in the 2.5-4.3V potential window; one after cycling at C/5 in the same potential window to see the impact of the increase of cycling rate and another one after cycling at C/5 in the larger potential window 2.5-4.6V to estimate the impact of higher states of charge (reaching higher delithiated compositions for the active material). Those electrodes were analysed after 50 cycles at end of discharge. A 900-5-air pristine electrode was also analysed as a matter of comparison.

As cycling was performed at 25°C in an electrolyte consisting of $LiPF_6$ in DMC and FEC, the analysis is focused on some elements, especially C and F, to study the apparition of the degradation products of the solvents and of lithium salts. Indeed, the degradation of $LiPF_6$ is expected to generate LiF and $Li_xPF_yO_z$-type species while the decomposition of the solvents will generate carbonaceous and oxygenated species.[47–53] It was shown that FEC could be quite unstable in $LiPF_6$-based electrolytes but mainly at high temperature (T > 45°C), so the degradation of FEC is expected to be limited in our case.[47–50] Regarding the DMC, it was shown that it could degrade at high potential leading to the formation of alkyl carbonates and

carbonated species and also react with deintercalated Li^+ ions to form lithium alkyl carbonates $ROCO_2Li$.[53,54]

The C1s, F1s, Li1s and O1s XPS spectra obtained are shown in Figure 8.

For the pristine electrode, in addition to the contributions previously described for the bare materials and according with the presence of electrode additives, two components in the C1s spectrum located at 286.5 eV and 291.0 eV are attributed to CH_2, and CF_2 environments of the PVDF binder. The signature of the carbon black in the electrode is well characterized by a set of black peaks corresponding to the XPS signal of our reference. The F1s spectrum is composed of two contributions, one from the PVDF binder located at 688.1 eV attributed to the CF_2 environments respectively and one contribution at 685.1 eV attributed to LiF.[43,44] In the Li1s peak, and, compared to the pristine material, we identify a new component under the Li1s peak according to LiF species at 56.3 eV in accordance with the LiF contribution in the F1s spectrum.

In addition to the contribution corresponding to O^{2-} anions in the NMC crystalline network (O_{NMC}) at 529.8 eV in the O1s spectra, two others components, mainly corresponding to the Li_2CO_3 oxygen atoms, are located at 531.9 eV and 533.4 eV. Compared to the Figure 5, we can note a decrease of the contribution of the O_{NMC} component in the O1s spectrum corresponding to the presence of oxygenated species coming from the electrode formulation.

After 50 cycles and whatever the cycling conditions, we observe an evolution in the core peaks spectra. In the F1s spectra, the cycling is concomitant with the appearance of a third component at 686.1 eV associated to the $Li_xPF_yO_z$ species coming from the electrolyte salt decomposition. A huge increase of the LiF components is also observed due to the electrolyte decomposition during cycling. Those new species induce an increase of the $LiF/Li_xPF_yO_z$ component in the Li1s spectra at 56.1 eV. The O1s and C1s spectra are also modified after cycling, due to the

degradation of electrolyte salt and solvents. For O1s spectra, the two peaks of the pristine material are still present, associated to the NMC oxygen atoms and Li_2CO_3 at 529.6 eV and 531.9 eV respectively. In this last peak, oxygen function linked to solvent degradation like CO_2 or O=C species are also included. Beside them, two new peaks are visible. Indeed, the apparition of fluorophosphates species is characterized by the peak at 534.2 eV, while the last component at 533.0 eV can be attributed to the C-O species.[43,44] This is consistent with the evolution of the contributions in the C1s spectra at 285.1 eV, 286.3 eV, 287.5 eV, 288.8 and 290.1 eV assigned to C-C/C-H, C-O, C=O, O-C=O and CO_3^{2-} environments respectively, linked to the solvents degradation, and confirm the attributions previously made.

The results obtained from the quantitative analysis (see Table S7 as an example) are gathered into 5 different categories:

- carbon black (comprising the as-named contributions in the C1s spectra);
- PVDF containing the PVDF contributions in C1s and F1s spectra;
- active material comprising the TM contributions and the NMC contributions in the O1s and Li1s spectra (O_{NMC} and Li_{NMC} respectively);
- $LiF/Li_xPF_yO_z$ species containing the LiF and $Li_xPF_yO_z$ contributions in Li1s, F1s and the phosphate contributions;
- and carbonaceous species comprising the remaining contributions in C1s spectra (i.e. contributions that are not in the carbon black or PVDF section), the remaining contributions in O1s spectra (i.e. contributions that are not NMC nor phosphate species) and the Li_2CO_3 contribution in Li1s spectra (Table S8 and Figure 9).

The decrease of carbon black and PVDF proportions from 25.1 at.% to 11.6 at.% and from 26.0 at.% to 15.8 at.% respectively between the pristine electrode and the electrode cycled at C/20 in

the 2.5-4.3V potential range reflects the covering of the electrode by degradation products after cycling. This decrease is not observed for the active material contributions because it is already covered by Li_2CO_3 in the pristine electrode and this Li_2CO_3 is dissolved during cycling and replaced by a SEI layer at the surface of the cycled electrodes. The proportion of carbonaceous species also decreases from 43.7 at.% to 34.1 at.% because of the important increase of $LiF/Li_xPF_yO_z$ proportion (from 2.7 at.% to 34.9 at.%) due to the electrolyte degradation. To get a better insight into the solvents degradation through the formation of carbonaceous species, their proportion compared to the rest of the C1s spectra was also determined. It increases from 33.8 at.% to 54.0 at.% illustrating the degradation of the solvents after cycling (Figure S10 and Table S8).

A decrease of carbon black and PVDF proportions from 11.6 at.% to 6.1 at.% and from 15.8 at.% to 11.0 at.% respectively (Table S8) is observed when the cycling rate is increased from C/20 to C/5. It shows that the electrode is more covered with SEI. Increasing the cycling rate generates a higher quantity of degradation products, especially $LiF/Li_xPF_yO_Z$ species as shown by the increase of their proportion from 34.9 at.% to 46.2 at.% in accordance with the increase of the $LiF/Li_xPF_yO_z$ contributions in the F1s and Li1s spectra (Table S8 and Figure 8b-c). And even if the global proportion of carbonaceous species slightly decreases from 34.1 at.% to 32.0 at.%, more carbonaceous species are formed when the cycling rate is increased from C/20 to C/5, as their proportion compared to the rest of the C1s spectra (SEI species in C1s) increases from 54.0 at.% to 65.0 at.% (see Figure S10 and Table S8). This increase is actually hidden by the more important increase of the $LiF/Li_xPF_yO_Z$ species contributions.

A significant amount of Li_2CO_3 (% C_{CO_3}) is detected at the surface of our electrode before cycling (4.3 at.%, see Figure S10) (as well as at the surface of our material initially, as shown by

the XPS analyses of the powders Table 2 and Table S6), but this amount is less important after cycling at C/20; 2.5-4.3V (1.5 at.%) and at C/5 (1.3 at.%) and at higher potential at 4.6V (1.2 at.%), showing that this carbonate is dissolved in the electrolyte during cycling.

When the potential window is enlarged from 2.5-4.3V to 2.5-4.6V for the C/5 cycling, the amount of degradation products decreases and the electrode is less covered with SEI. Indeed, the carbon black and PVDF proportions increase from 6.1 at.% to 8.4 at.% and from 11.0 at.% to 21.5 at.% respectively, while the proportions of $LiF/Li_xPF_yO_z$ species and carbonaceous species decrease from 46.2 at.% to 37.6 at.% and from 32.0 at.% to 28.9 at.% respectively (Table S8).

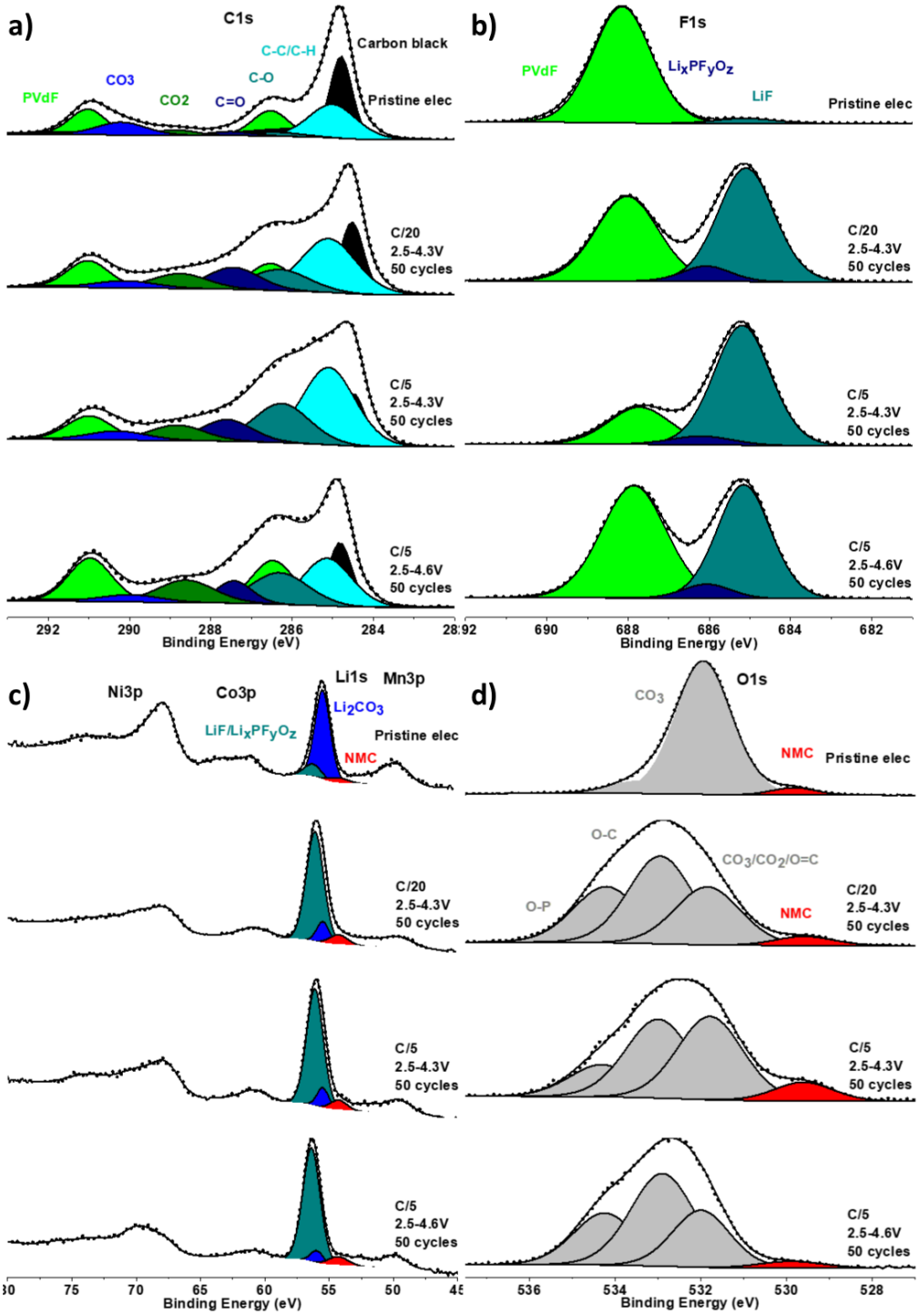

Figure 8. C1s (a), F1s (b) Li1s, Ni3p, Co3p, Mn3p (c) and O1s (d) XPS spectra of the 900-5-air pristine electrode and 900-5-air electrodes cycled for 50 cycles at C/20 between 2.5 and 4.3V, at C/5 between 2.5 and 4.3V and at C/5 between 2.5 and 4.6V. The dots represent the experimental data and the lines the fitted spectra.

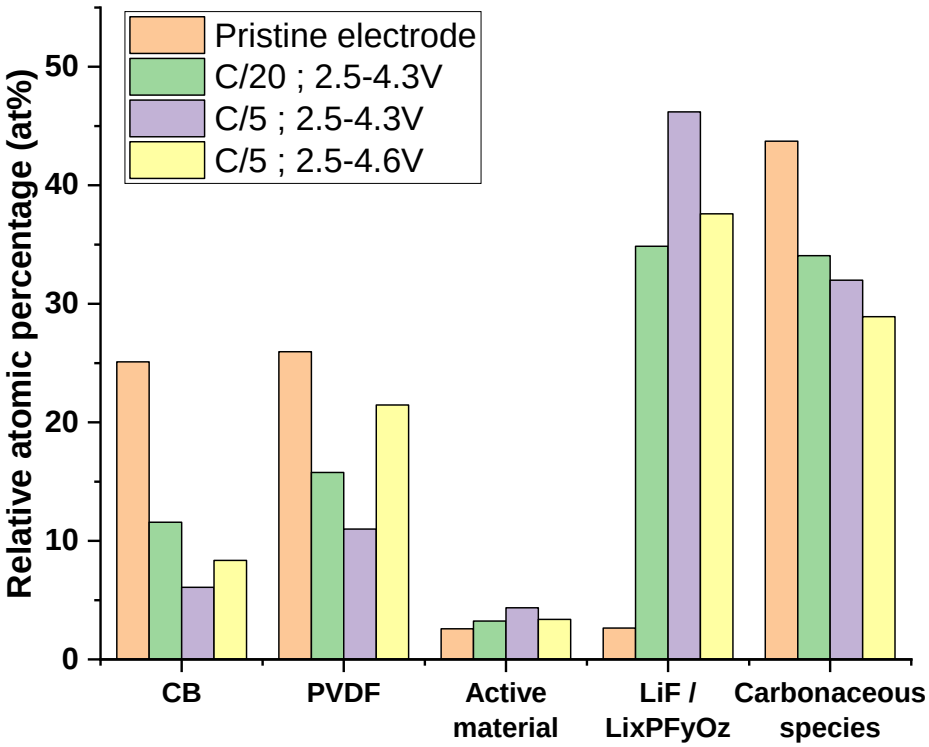

Figure 9. Evolution of atomic percentages (at. %) of carbon black (CB), PVDF, active material, LiF / $Li_xPF_yO_z$ species and carbonaceous species at the surface of 900-5-air pristine electrodes and electrodes cycled for 50 cycles at C/20 2.5-4.3V; C/5 2.5-4.3V and C/5 2.5-4.6V.

Finally, to investigate the influence of the primary particle size on the electrode/electrolyte interface composition, XPS analyses were performed on electrodes with the 170 nm primary particles (810-5-air), 400 nm primary particles (900-5-air) and 1.2 µm primary particles (930-5-air). The electrodes were analysed after cycling at C/5 in the 2.5-4.6V potential window after 50 cycles at end of discharge. The corresponding pristine electrodes were also analysed as a matter of comparison. The spectra and results of the quantitative analyses are given in Figures 10, S11, S12 and Table S9. The decrease of the relative atomic percentages of carbon black and PVDF

contributions between the pristine and the cycled electrodes (from 25.1 at.% to 8.4 at.% and from 26.0 at.% to 21.5 at.% respectively for the 900-5-air sample for example) reflects the covering of the electrodes by the degradation products formed after cycling. Regarding the SEI composition, it is shown that a higher quantity of $LiF/Li_xPF_yO_z$ species is formed at the surface of the 400 nm particles (900-5-air sample) and 1.2 µm particles (930-5-air sample) after cycling (37.6 at.% and 36.7 at.% respectively versus 30.4 at.% for the 810-5-air cycled electrode). As a consequence of this higher amount of $LiF/Li_xPF_yO_z$ species, a lower amount of carbonaceous species is observed at the surface of the cycled electrodes with 400 nm and 1.2 µm particles (28.9 at.% and 28.6 at.% respectively versus 32.7 at.% for the 810-5-air cycled electrode) (Figure 10 and Table S9). However, the more important proportion of carbonaceous species compared to the rest of the C1s spectra (SEI species in C1s) for the 3 cycled electrodes compared to their pristine counterparts reflects the degradation of the solvents through the generation of carbonaceous products (from 33.8 at.% for the pristine electrode to 49.2 at.% for the cycled electrode of the 900-5-air sample for example, see Figure S12 and Table S9). As previously, a significant amount of Li_2CO_3 (% C CO_3) is detected at the surface of the electrodes before cycling (4.3 at.% for the 900-5-air sample for example, see Figure S12 and Table S9) but this amount is less important after cycling at C/5 in the 2.5-4.6V potential range (1.2 at.% for the 900-5-air sample for example) showing that this carbonate is dissolved in the electrolyte during cycling.

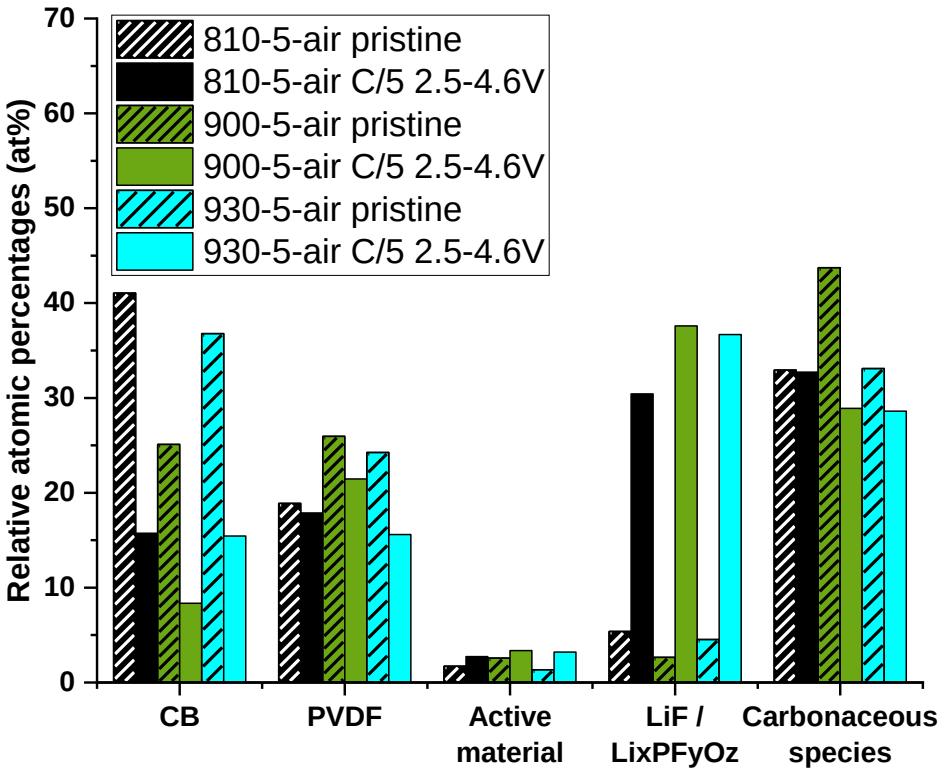

Figure 10. Evolution of atomic percentage (at. %) of carbon black (CB), PVDF, active material, $LiF/Li_xPF_yO_z$ species and carbonaceous species at the surface of 810-5-air, 900-5-air, 930-5-air electrodes cycled for 50 cycles at C/5 in the 2.5-4.6V potential range and their corresponding pristine electrodes.

Discussion

Effect of particle size on the electrochemical performances and reactivity versus electrolyte

The kinetics of the Li^+ deintercalation and reintercalation can be affected by two obvious factors as illustrated by the results discussed in Figure 6: (i) the amount of Ni^{2+} ions localized in the interslab spaces and (ii) the particle size. The first penalizes fast Li^+ ions diffusion in the

interslab spaces and the second increases the diffusion length for Li^+ ions. The "5-O_2" samples with lower amount of Ni^{2+} ions in interslab spaces (1.5-1.8%) show higher reversible capacities compared to the "5-air" samples which contain between 2.3 and 3.8% of Ni^{2+} ions in Li sites. However, this beneficial effect of the lower amount of Ni^{2+} ions in Li sites is only critical for samples with particles sizes smaller than 810 nm. For larger sizes, the diffusion length becomes the limiting factor, as observed for instance for the 930-5-O_2 sample with only 1.8% Ni^{2+} ions in Li sites but 2.1 μm primary particles, and thus lower 1st discharge capacity (Table 4, Figure S6), and as also reported by Wang et al.[11] and by Li et al.[13] Indeed, as the particle size grows, the Li^+ ion diffusion path gets longer and more Li^+ ions are trapped at the centre of the particles, becoming electrochemically inactive and leading to a reduction of the reversible discharge capacities. Furthermore, increasing the particle size allows the decrease of the specific surface area to limit the parasitic reactions at the electrode/electrolyte interface, reducing in consequence the amount of resistive degradation products formed in the SEI and the charge transfer resistance at the interface. It also implies less Li^+ ions lost in the formation of degradation products such as LiF/$Li_xPF_yO_z$ species composing the SEI, and thus more Li^+ ions remaining electrochemically active. Indeed, a decrease of the irreversible capacity at the end of the first cycle (IRC, %) is observed, from 21% to 11% when increasing the particle size from 170 nm (810-5-air sample) to 400 nm (900-5-air sample), as well as a significant increase in discharge capacities from 149 mAh/g to 165 mAh/g (Table 4). As shown previously, thicker Li_2CO_3 layers are found at the surface of larger particles (see Table S6). This Li_2CO_3 tends to react in $LiPF_6$-based electrolyte to form LiF.[55] This implies an increasing amount of LiF/$Li_xPF_yO_z$ species at the surface of the largest particles after cycling, as shown in Figure 10. As LiF is highly ionically resistive[56–59], it participates also to an increasing resistivity, to a lower Li^+ ions diffusion through the

electrode/electrolyte interface, and thus to a rapid decrease of the reversible discharge capacities for the largest particles (Table 5).

This study demonstrates that in-depth characterization of the samples (structure, morphology, surface composition) is highly useful to predict and optimize the performance in Li-ion batteries. Indeed, Ronduda et al. had also studied the impact of the calcination temperature on the structure and morphology of NMC622.[10] They obtained a series of samples with particle sizes ranging from 100 nm to 1.2 µm, but with very different and rather large amounts of Ni^{2+} ions in Li sites. They were thus not able to discriminate between the effect of the particle size and that of the dimensionality of the structure, for cycling conditions such as C/20 between 2.8 and 4.4V.

Effect of the increase of cycling rate on the electrochemical performances and the reactivity versus electrolyte

The detrimental effect of the increase of the Li^+ ions diffusion path, observed when the particle size is increased up to more than 1 µm, is exacerbated for cycling performed at higher rate. It is shown for instance for the 1.2 µm particles (930-5-air sample) by the large decrease of the 1st discharge capacity from 165 to 87 mAh/g and the increase of IRC from 13 to 30% when the cycling rate is changed from C/20 to C/5 (Table 5). Such a drastic drop of performance is also observed for the smallest 170 nm particles (810-5-air sample), with the decrease of capacity from 149 to 119 mAh/g and the increase of IRC from 21 to 34% (Table 5). In that case, the formation of a thicker resistive layer is observed due to an exacerbated decomposition of the electrolyte for those particles showing higher specific surface area. Indeed, the XPS results given in Figure 9 and Table S8 show a clear decrease of the carbon black and PVDF contributions (from 11.6 at.%

to 6.1 at.% and from 15.8 at.% to 11.0 at.% respectively) for the 900-5-air (400 nm particles) cycled electrodes when increasing the cycling rate from C/20 to C/5. Such result illustrates a more important particles covering with degradation products. The large increase of the $LiF/Li_xPF_yO_z$ proportion from 34.9 at.% to 46.2 at.% (Figure 9 and Table S8) and that of carbonaceous species in C1s spectra from 54.0 at.% to 65.0 at.% (Figure S10 and Table S8) reveal that higher cycling rate favours the degradation of the solvents and, to a greater extent, of the electrolyte salt.[47,49–52]

Effect of the increase of cut-off voltage on the electrochemical performances and the reactivity versus electrolyte

In the 2.5-4.6V potential window, the 400 nm primary particles (900-5-air electrodes) deliver the best initial capacity, as in the 2.5-4.3V potential window, but have a declining capacity retention as shown in Figure S9. After 5 activation cycles, larger capacities are delivered by the 200 nm particles (840-5-air electrodes). More reactivity detrimental to the capacity retention could have been expected for smaller particles, but it is not the case as shown by their very good capacity retention. Upon cycling at higher cut-off potential, the materials go through higher deintercalation states at end of charge and are thus prone to undergo more important volume changes due to the successive deintercalation and reintercalation of Li^+ ions (as discussed in details in Figure S13). Those volume changes are expected to be amplified and thus detrimental to capacity retention upon long range cycling for larger particles (here for the 400 nm particles of the 900-5-air sample versus the 200 nm ones of the 840-5-air sample).

Concerning the nature of the solid-liquid interface, the decrease of the proportion of $LiF/Li_xPF_yO_z$ from 46.2 at.% to 37.6 at.% observed at the surface of the 900-5-air electrodes (400 nm particles) when increasing the cut-off voltage from 4.3V to 4.6V (Figure 9 and Table S8) is in accordance with previous works.[59,60] As the amount of settled LiF would decrease during the charge process, its amount at the surface of the positive electrode decreases when cycling is performed at higher cut-off voltage.[59,60] Indeed, apart from the decomposition of $LiPF_6$ at the positive electrode surface[50], LiF can also be formed at the Li metal negative electrode and migrate from the negative to the positive electrode during discharge so it was shown that LiF would preferentially settle on the positive electrode during discharge.[61] Moreover, it was shown that increasing the charge voltage up to 4.5V could cause a decomposition / dissolution of the SEI layer with a vanishing of the spectral features originated from the degradation products of the electrolyte salt and organic solvents, with no noticeable change in the surface chemistry of the NMC material.[60] This SEI layer dissolution could be caused by weakening or breaking of chemical bonds due to mechanical stresses induced by lattice volume changes, that tend, as just discussed, to be larger when cycling is performed at higher voltages due to the larger amount of deintercalated Li^+ ions. This is also in accordance with the decrease of the proportion of carbonaceous species from 32.0 at.% to 28.9 at.% observed for these 900-5-air electrodes (400 nm particles) when increasing the cut-off voltage from 4.3V to 4.6V (Figure 9 and Table S8).

As a conclusion, an optimum for the particles size has obviously always to be found in order to find the good balance between the limitation of the reactivity on one side, by increasing the particle size, and the minimization of the diffusion path on the other side, by decreasing the particle size. From those results, an optimum primary particle size of 400 nm can be inferred for cycling performed up to 4.3V, the 900-5-air sample delivering the highest reversible capacities

and best capacity retentions regardless of the cycling rate. For cycling performed at higher cut-off potentials up to 4.6V, the optimum primary particle size would rather be 200 nm. Smaller primary particles should prevail upon others for cycling at high potential as they have better capacity retention than larger primary particles, as shown by the very good capacity retention of the 170 nm particles. It thus appears that samples with primary particles between 200 and 400 nm are the most versatile as they deliver the best performances regardless of the cycling conditions. To optimize the performance of the materials, the amount of Ni^{2+} ions in the interslab spaces has to be lowered to less than 2 % and that of Li_2CO_3 at the surface to less than 5 at.%, by performing the lithiation under O_2 atmosphere with an excess of Li limited to 1 wt.%. Those results show that the cycling conditions can affect significantly the reactivity of the materials versus the electrolyte and the composition of the positive electrode/electrolyte interface. Increasing the cycling rate from C/20 to C/5 in the 2.5-4.3V potential window enhances the formation of degradation products of the solvents (carbonaceous and oxygenated species) and, to a greater degree, degradation products of $LiPF_6$ (LiF and $Li_xPF_yO_z$ species). Enlarging the potential window from 2.5-4.3V to 2.5-4.6V at the same cycling rate reduces the proportion of $LiF/Li_xPF_yO_z$ species at the surface and increases that of carbonaceous species, resulting from the solvents degradation, DMC and FEC.

CONCLUSION

The parameters of a two-step synthesis consisting of a coprecipitation of the transition metal precursor, followed by a solid-state reaction with Li_2CO_3 have been investigated to obtain NMC622 layered oxides. Samples with crystallographic structure close to the ideal 2D layered

structure (less than 3.8% Ni^{2+} ions in Li^{+} sites) and with variable primary particle sizes from 170 nm to 2 µm were obtained. Larger primary particles are obtained when the lithiation temperature is increased up to 930°C, the lithium carbonate excess minimized to 1 wt. % and the thermal treatment carried out under O_2 flow. The amount of Ni^{2+} ions in Li^{+} sites of NMC622 can be minimized until less than 1.8% by doing the lithiation under O_2 flow, the oxidant atmosphere disfavouring the stabilisation of nickel ions at the divalent oxidation state. The decrease of the amount of Li_2CO_3 at the surface of the particles can be achieved by minimizing the excess used for lithiation or by doing the lithiation under O_2 flow. In terms of particle size, an optimum has to be found. On one hand, increasing the particle size enables to decrease the interfacial area with the electrolyte and limit the parasitic reactions. It also decreases the number of grain boundaries that hinders Li^{+} ions diffusion so the performances are significantly enhanced. On the other hand, too large particles are detrimental for the performances because of their larger diffusion path for Li^{+} ions and of their tendency to form higher amounts of highly resistive LiF at the electrode/electrolyte interface during cycling, as a consequence of the larger amount of Li_2CO_3 located at their surface in their pristine state. An optimum primary particle size of 400 nm can be inferred for cyclings performed up to 4.3V, those particles delivering the highest reversible capacities and best capacity retentions regardless of the cycling rate. For cyclings performed at higher cut-off potentials up to 4.6V, the optimum primary particle size would rather be 200 nm, those particles having better capacity retention than larger primary particles. The cycling conditions have a significant influence on the electrode/electrolyte interface composition after cycling. Increasing the cycling rate from C/20 to C/5 enhances the formation of $LiF/Li_xPF_yO_z$ species at the surface of 400 nm particles which is an evidence of a more important degradation of $LiPF_6$. Increasing the potential window from 2.5-4.3V to 2.5-4.6V reduces the proportion of

$LiF/Li_xPF_yO_z$ species in favour of carbonaceous species that are degradation products of the solvents used in the electrolyte, DMC and FEC in our case. As a conclusion, particles between 200 and 400 nm must be preferred as they deliver the best performances regardless of the cycling conditions and do not generate a too large amount of degradation products at the positive electrode/electrolyte interface.

ASSOCIATED CONTENT

Supporting information

The Supporting information contains figures, tables and description to complete and precise some points in the main manuscript. This material is available free of charge via the Internet at http://pubs.acs.org.

AUTHOR INFORMATION

Corresponding author

* Laurence Croguennec

Laurence.Croguennec@icmcb.cnrs.fr

Funding Sources

This work was funded by Saft and Région Nouvelle Aquitaine.

ACKNOWLEDGMENT

The authors acknowledge Saft and Région Nouvelle-Aquitaine for the funding of the project, as well as the French National Research Agency (STORE-EX Labex Project ANR-10-LABX-76-01) for financial support for their research on the electrochemical energy storage. The authors thank Cathy Denage, Laëtitia Etienne, Eric Lebraud and Dominique Denux at ICMCB for their technical support for ICP-OES, granulometry, XRD and TGA-MS analyses. The authors also

thank Philippe Legros at PLACAMAT and Marie-Anne Dourges at ISM for their scientific support with SEM and BET analyses.

REFERENCES

(1) Noh, H.-J.; Youn, S.; Yoon, C. S.; Sun, Y.-K. Comparison of the Structural and Electrochemical Properties of Layered $Li[Ni_xCo_yMn_z]O_2$ (x = 1/3, 0.5, 0.6, 0.7, 0.8 and 0.85) Cathode Material for Lithium-Ion Batteries. *J. Power Sources* **2013**, *233*, 121-130.

(2) Kim, M.-H.; Shin, H.-S.; Shin, D.; Sun, Y.-K. Synthesis and Electrochemical Properties of $Li[Ni_{0.8}Co_{0.1}Mn_{0.1}]O_2$ and $Li[Ni_{0.8}Co_{0.2}]O_2$ via Co-Precipitation. *J. Power Sources* **2006**, *159* (2), 1328-1333.

(3) Lee, K.-S.; Myung, S.-T.; Amine, K.; Yashiro, H.; Sun, Y.-K. Structural and Electrochemical Properties of Layered $Li[Ni_{1-2x}Co_xMn_x]O_2$ (X=0.1-0.3) Positive Electrode Materials for Li-Ion Batteries. *J. Electrochem. Soc.* **2007**, *154* (10), A971-A977.

(4) Ohzuku, T.; Makimura, Y. Layered Lithium Insertion Material of $LiCo_{1/3}Ni_{1/3}Mn_{1/3}O_2$ for Lithium-Ion Batteries. *Chem. Lett.* **2001**, *30* (7), 642-643.

(5) Wang, Y.; Jiang, J.; Dahn, J. R. The Reactivity of Delithiated $Li(Ni_{1/3}Co_{1/3}Mn_{1/3})O_2$, $Li(Ni_{0.8}Co_{0.15}Al_{0.05})O_2$ or $LiCoO_2$ with Non-Aqueous Electrolyte. *Electrochem. Commun.* **2007**, *9* (10), 2534-2540.

(6) Liang, L.; Du, K.; Peng, Z.; Cao, Y.; Duan, J.; Jiang, J.; Hu, G. Co-Precipitation Synthesis of $Ni_{0.6}Co_{0.2}Mn_{0.2}(OH)_2$ Precursor and Characterization of $LiNi_{0.6}Co_{0.2}Mn_{0.2}O_2$ Cathode Material for Secondary Lithium Batteries. *Electrochim. Acta* **2014**, *130*, 82-89.

(7) Zybert, M.; Ronduda, H.; Szczęsna, A.; Trzeciak, T.; Ostrowski, A.; Żero, E.; Wieczorek, W.; Raróg-Pilecka, W.; Marcinek, M. Different Strategies of Introduction of Lithium Ions into Nickel- manganese- cobalt Carbonate Resulting in $LiNi_{0.6}Mn_{0.2}Co_{0.2}O_2$ (NMC622) Cathode Material for Li-Ion Batteries. *Solid State Ionics* **2020**, *348*, 115273.

(8) Ma, Y.; Li, L.; Wang, L.; Luo, R.; Xu, S.; Wu, F.; Chen, R. Effect of Metal Ion Concentration in Precursor Solution on Structure and Electrochemical Performance of $LiNi_{0.6}Co_{0.2}Mn_{0.2}O_2$. *J. Alloys Compd.* **2019**, *778*, 643-651.

(9) Li, F.; Liu, Z.; Shen, J.; Xu, X.; Zeng, L.; Li, Y.; Zhang, D.; Zuo, S.; Liu, J. Ni-Rich Layered Oxide with Preferred Orientation (110) Plane as a Stable Cathode Material for High-Energy Lithium-Ion Batteries. *Nanomaterials* **2020**, *10* (12), 2495.

(10) Ronduda, H.; Zybert, M.; Szczęsna-Chrzan, A.; Trzeciak, T.; Ostrowski, A.; Szymański, D.; Wieczorek, W.; Raróg-Pilecka, W.; Marcinek, M. On the Sensitivity of the Ni-Rich Layered Cathode Materials for Li-Ion Batteries to the Different Calcination Conditions. *Nanomaterials* **2020**, *10* (10), 2018.

(11) Wang, L.; Wu, B.; Mu, D.; Liu, X.; Peng, Y.; Xu, H.; Liu, Q.; Gai, L.; Wu, F. Single-Crystal $LiNi_{0.6}Co_{0.2}Mn_{0.2}O_2$ as High Performance Cathode Materials for Li-Ion Batteries. *J. Alloys Compd.* **2016**, *674*, 360-367.

(12) Xia, Y.-F.; Nie, M.; Wang, Z.-B.; Yu, F.-D.; Zhang, Y.; Zheng, L.-L.; Wu, J.; Ke, K. Structural, Morphological and Electrochemical Investigation of $LiNi_{0.6}Co_{0.2}Mn_{0.2}O_2$ Cathode Material Synthesized in Different Sintering Conditions. *Ceram. Int.* **2015**, *41* (9), 11815-11823.

(13) Li, H.; Li, J.; Ma, X.; Dahn, J. R. Synthesis of Single Crystal $LiNi_{0.6}Mn_{0.2}Co_{0.2}O_2$ with Enhanced Electrochemical Performance for Lithium Ion Batteries. *J. Electrochem. Soc.* **2018**, *165* (5), A1038-A1045.

(14) Delmas, C.; Ménétrier, M.; Croguennec, L.; Saadoune, I.; Rougier, A.; Pouillerie, C.; Prado, G.; Grüne, M.; Fournès, L. An Overview of the $Li(Ni,M)O_2$ Systems: Syntheses, Structures and Properties. *Electrochim. Acta* **1999**, *45* (1-2), 243-253.

(15) Delmas, C.; Croguennec, L. Layered $Li(Ni, M)O_2$ Systems as the Cathode Material in Lithium-Ion Batteries. *MRS Bull.* **2002**, *27* (8), 608-612.

(16) Croguennec, L.; Palacin, M. R. Recent Achievements on Inorganic Electrode Materials for Lithium-Ion Batteries. *J. Am. Chem. Soc.* **2015**, *137* (9), 3140-3156.

(17) Ju, X.; Huang, H.; He, W.; Zheng, H.; Deng, P.; Li, S.; Qu, B.; Wang, T. Surfactant-Assisted Synthesis of High Energy {010} Facets Beneficial to Li-Ion Transport Kinetics with Layered $LiNi_{0.6}Co_{0.2}Mn_{0.2}O_2$. *ACS Sustainable Chem. Eng.* **2018**, *6* (5), 6312-6320.

(18) Jiang, M.; Zhang, Q.; Wu, X.; Chen, Z.; Danilov, D. L.; Eichel, R.-A.; Notten, P. H. L. Synthesis of Ni-Rich Layered-Oxide Nanomaterials with Enhanced Li-Ion Diffusion Pathways as High-Rate Cathodes for Li-Ion Batteries. *ACS Appl. Energy Mater.* **2020**, *3* (7), 6583-6590.

(19) Zhu, J.; Chen, G. Single-Crystal Based Studies for Correlating the Properties and High-Voltage Performance of $Li[Ni_xMn_yCo_{1-x-y}]O_2$ Cathodes. *J. Mater. Chem. A* **2019**, *7* (10), 5463-5474.

(20) Li, J.; Camardese, J.; Glazier, S.; Dahn, J. R. Structural and Electrochemical Study of the Li-Mn-Ni Oxide System within the Layered Single Phase Region. *Chem. Mater.* **2014**, *26* (24), 7059-7066.

(21) Li, J.; Cameron, A. R.; Li, H.; Glazier, S.; Xiong, D.; Chatzidakis, M.; Allen, J.; Botton, G. A.; Dahn, J. R. Comparison of Single Crystal and Polycrystalline $LiNi_{0.5}Mn_{0.3}Co_{0.2}O_2$ Positive Electrode Materials for High Voltage Li-Ion Cells. *J. Electrochem. Soc.* **2017**, *164* (7), A1534-A1544.

(22) Liu, G.; Li, M.; Wu, N.; Cui, L.; Huang, X.; Liu, X.; Zhao, Y.; Chen, H.; Yuan, W.; Bai, Y. Single-Crystalline Particles: An Effective Way to Ameliorate the Intragranular Cracking, Thermal Stability, and Capacity Fading of the $LiNi_{0.6}Co_{0.2}Mn_{0.2}O_2$ Electrodes. *J. Electrochem. Soc.* **2018**, *165* (13), A3040-A3047.

(23) Heenan, T. M. M.; Wade, A.; Tan, C.; Parker, J. E.; Matras, D.; Leach, A. S.; Robinson, J. B.; Llewellyn, A.; Dimitrijevic, A.; Jervis, R.; Quinn, P. D.; Brett, D. J. L.; Shearing, P. R. Identifying the Origins of Microstructural Defects Such as Cracking within Ni- Rich NMC811 Cathode Particles for Lithium- Ion Batteries. *Adv. Energy Mater.* **2020**, *10* (47), 2002655.

(24) Li, J.; Li, H.; Stone, W.; Weber, R.; Hy, S.; Dahn, J. R. Synthesis of Single Crystal $LiNi_{0.5}Mn_{0.3}Co_{0.2}O_2$ for Lithium Ion Batteries. *J. Electrochem. Soc.* **2017**, *164* (14), A3529-A3537.

(25) Pajot, S.; Feydi, P.; Weill, F.; Ménétrier, M.; Yildirim, G.; Simonin, L.; Croguennec, L. Synthesis of Li and Mn-Rich Layered Oxides as Concentration-Gradients for Lithium-Ion Batteries. *J. Electrochem. Soc.* **2018**, *165* (3), A425-A433.

(26) Rodriguez-Carvajal, J. Recent Advances in Magnetic Structure Determination by Neutron Powder Diffraction. *Physica B* **1993**, *192*, 55-69.

(27) Rodriguez-Carvajal, J. Https://Www-Llb.Cea.Fr/Fullweb/Powder.Htm. Laboratoire Léon Brillouin (CEA-CNRS).

(28) Scofield, J. H. Hartree-Slater Subshell Photoionization Cross-Sections at 1254 and 1487 eV. *J. Electron. Spectrosc. Relat. Phenom.* **1976**, *8*, 129-137.

(29) Cao, H.; Zhang, Y.; Zhang, J.; Xia, B. Synthesis and Electrochemical Characteristics of Layered LiNiCoMnO Cathode Material for Lithium Ion Batteries. *Solid State Ionics* **2005**, *176* (13-14), 1207-1211.

(30) Ban, C.; Li, Z.; Wu, Z.; Kirkham, M. J.; Chen, L.; Jung, Y. S.; Payzant, E. A.; Yan, Y.; Whittingham, M. S.; Dillon, A. C. Extremely Durable High-Rate Capability of a $LiNi_{0.4}Mn_{0.4}Co_{0.2}O_2$ Cathode Enabled with Single-Walled Carbon Nanotubes. *Adv. Energy Mater.* **2011**, *1*, 58-62.

(31) Hartmann, L.; Pritzl, D.; Beyer, H.; Gasteiger, H. A. Evidence for Li^+/H^+ Exchange during Ambient Storage of Ni-Rich Cathode Active Materials. *J. Electrochem. Soc.* **2021**, *168*, 070507.

(32) Martinez, A. C.; Grugeon, S.; Cailleu, D.; Courty, M.; Tran-Van, P.; Delobel, B.; Laruelle, S. High Reactivity of the Nickel-Rich $LiNi_{1-x-y}Mn_xCo_yO_2$ Layered Materials Surface

towards H_2O/CO_2 Atmosphere and $LiPF_6$-Based Electrolyte. *J. Power Sources* **2020**, *468*, 228204.

(33) Busà, C.; Belekoukia, M.; Loveridge, M. J. The Effects of Ambient Storage Conditions on the Structural and Electrochemical Properties of NMC-811 Cathodes for Li-Ion Batteries. *Electrochim. Acta* **2021**, *366*, 137358.

(34) Rougier, A.; Gravereau, P.; Delmas, C. Optimization of the Composition of the $Li_{1-z}Ni_{1+z}O_2$ Electrode Materials: Structural, Magnetic, and Electrochemical Studies. *J. Electrochem. Soc.* **1996**, *143* (4), 1168-1175.

(35) Wang, T.; Ren, K.; Xiao, W.; Dong, W.; Qiao, H.; Duan, A.; Pan, H.; Yang, Y.; Wang, H. Tuning the Li/Ni Disorder of the NMC811 Cathode by Thermally Driven Competition between Lattice Ordering and Structure Decomposition. *J. Phys. Chem. C* **2020**, *124* (10), 5600-5607.

(36) Peres, J. P.; Delmas, C.; Rougier, A.; Broussely, M.; Perton, F.; Biensan, P.; Willmann, P. The Relationship between the Composition of Lithium Nickel Oxide and the Loss of Reversibility during the First Cycle. *J. Phys. Chem. Solids* **1996**, *57* (6-8), 1057-1060.

(37) Wang, D.; Xin, C.; Zhang, M.; Bai, J.; Zheng, J.; Kou, R.; Peter Ko, J. Y.; Huq, A.; Zhong, G.; Sun, C.-J.; Yang, Y.; Chen, Z.; Xiao, Y.; Amine, K.; Pan, F.; Wang, F. Intrinsic Role of Cationic Substitution in Tuning Li/Ni Mixing in High-Ni Layered Oxides. *Chem. Mater.* **2019**, *31* (8), 2731-2740.

(38) Yin, S.-C.; Rho, Y.-H.; Swainson, I.; Nazar, L. F. X-Ray/Neutron Diffraction and Electrochemical Studies of Lithium De/Re-Intercalation in $Li_{1-x}Co_{1/3}Ni_{1/3}Mn_{1/3}O_2$ (x=0→1). *Chem. Mater.* **2006**, *18* (7), 1901-1910.

(39) Guilmard, M.; Pouillerie, C.; Croguennec, L.; Delmas, C. Structural and Electrochemical Properties of $LiNi_{0.70}Co_{0.15}Al_{0.15}O_2$. *Solid State Ionics* **2003**, *160*, 39-50.

(40) Guilmard, M.; Croguennec, L.; Delmas, C. Effects of Manganese Substitution for Nickel on the Structural and Electrochemical Properties of $LiNiO_2$. *J. Electrochem. Soc.* **2003**, *150* (10), A1287.

(41) Guilmard, M.; Rougier, A.; Grüne, M.; Croguennec, L.; Delmas, C. Effects of Aluminum on the Structural and Electrochemical Properties of $LiNiO_2$. *J. Power Sources* **2003**, *115*, 305-314.

(42) Croguennec, L.; Suard, E.; Willmann, P.; Delmas, C. Structural and Electrochemical Characterization of the $LiNi_{1-y}Ti_yO_2$ Electrode Materials Obtained by Direct Solid-State Reactions. *Chem. Mater.* **2002**, *14*, 2149-2157.

(43) Gauthier, N.; Courrèges, C.; Demeaux, J.; Tessier, C.; Martinez, H. Influence of the Cathode Potential on Electrode Interactions within a $Li_4Ti_5O_{12}$ vs $LiNi_{3/5}Mn_{1/5}Co_{1/5}O_2$ Li-Ion Battery. *J. Electrochem. Soc.* **2020**, *167* (4), 040504.

(44) Karayaylali, P.; Zhang, Y.; Giordano, L.; Katayama, Y.; Tatara, R.; Yu, Y.; Maglia, F.; Jung, R.; Shao-Horn, Y. The Role of Diphenyl Carbonate Additive on the Interfacial Reactivity of Positive Electrodes in Li-Ion Batteries. *J. Electrochem. Soc.* **2020**, *167* (4), 040522.

(45) Dahéron, L.; Dedryvère, R.; Martinez, H.; Ménétrier, M.; Denage, C.; Delmas, C.; Gonbeau, D. Electron Transfer Mechanisms upon Lithium Deintercalation from $LiCoO_2$ to CoO_2 Investigated by XPS. *Chem. Mater.* **2008**, *20* (2), 583-590.

(46) Dedryvère, R.; Foix, D.; Franger, S.; Patoux, S.; Daniel, L.; Gonbeau, D. Electrode/Electrolyte Interface Reactivity in High-Voltage Spinel $LiMn_{1.6}Ni_{0.4}O_4/Li_4Ti_5O_{12}$ Lithium-Ion Battery. *J. Phys. Chem. C* **2010**, *114* (24), 10999-11008.

(47) Shin, H.; Park, J.; Sastry, A. M.; Lu, W. Effects of Fluoroethylene Carbonate (FEC) on Anode and Cathode Interfaces at Elevated Temperatures. *J. Electrochem. Soc.* **2015**, *162* (9), A1683-A1692.

(48) Zhang, S. S. A Review on Electrolyte Additives for Lithium-Ion Batteries. *J. Power Sources* **2006**, *162* (2), 1379-1394.

(49) Kim, K.; Park, I.; Ha, S.-Y.; Kim, Y.; Woo, M.-H.; Jeong, M.-H.; Shin, W. C.; Ue, M.; Hong, S. Y.; Choi, N.-S. Understanding the Thermal Instability of Fluoroethylene Carbonate in $LiPF_6$-Based Electrolytes for Lithium Ion Batteries. *Electrochim. Acta* **2017**, *225*, 358-368.

(50) Tasaki, K.; Goldberg, A.; Lian, J.-J.; Walker, M.; Timmons, A.; Harris, S. J. Solubility of Lithium Salts Formed on the Lithium-Ion Battery Negative Electrode Surface in Organic Solvents. *J. Electrochem. Soc.* **2009**, *156* (12), A1019-A1027.

(51) Sinha, N. N.; Burns, J. C.; Dahn, J. R. Storage Studies on Li/Graphite Cells and the Impact of So-Called SEI-Forming Electrolyte Additives. *J. Electrochem. Soc.* **2013**, *160* (4), A709-A714.

(52) Deng, B.; Li, J.; Shang, H.; Liu, W.; Wan, Q.; Chen, M.; Qu, M.; Peng, G. Improving Cyclic Stability of $LiNi_{0.6}Co_{0.2}Mn_{0.2}O_2$-$SiO_x$/Graphite Full Cell Using Tris(Trimethylsilyl)Phosphite and Fluoroethylene Carbonate as Combinative Electrolyte Additive. *Ionics* **2020**, *26*, 2247-2257.

(53) Dedryvère, R.; Gireaud, L.; Grugeon, S.; Laruelle, S.; Tarascon, J.-M.; Gonbeau, D. Characterization of Lithium Alkyl Carbonates by X-Ray Photoelectron Spectroscopy: Experimental and Theoretical Study. *J. Phys. Chem. B* **2005**, *109* (33), 15868-15875.

(54) Moshkovich, M.; Cojocaru, M.; Gottlieb, H. E.; Aurbach, D. The Study of the Anodic Stability of Alkyl Carbonate Solutions by in Situ FTIR Spectroscopy, EQCM, NMR and MS. *J. Electroanal. Chem.* **2001**, *497* (1-2), 84-96.

(55) Freiberg, A. T. S.; Sicklinger, J.; Solchenbach, S.; Gasteiger, H. A. Li_2CO_3 Decomposition in Li-Ion Batteries Induced by the Electrochemical Oxidation of the Electrolyte and of Electrolyte Impurities. *Electrochim. Acta* **2020**, *346*, 136271.

(56) Lin, F.; Markus, I. M.; Nordlund, D.; Weng, T.-C.; Asta, M. D.; Xin, H. L.; Doeff, M. M. Surface Reconstruction and Chemical Evolution of Stoichiometric Layered Cathode Materials for Lithium-Ion Batteries. *Nat. Commun.* **2014**, *5*, 3529.

(57) Aurbach, D.; Weissman, I.; Schechter, A.; Cohen, H. X-Ray Photoelectron Spectroscopy Studies of Lithium Surfaces Prepared in Several Important Electrolyte Solutions. A Comparison with Previous Studies by Fourier Transform Infrared Spectroscopy. *Langmuir* **1996**, *12* (16), 3991-4007.

(58) Aurbach, D.; Ein- Eli, Y.; Markovsky, B.; Zaban, A.; Luski, S.; Carmeli, Y.; Yamin, H. The Study of Electrolyte Solutions Based on Ethylene and Diethyl Carbonates for Rechargeable Li Batteries: II. Graphite Electrodes. *J. Electrochem. Soc.* **1995**, *142* (9), 2882-2890.

(59) Wang, W.; Yang, Q.; Qian, K.; Li, B. Impact of Evolution of Cathode Electrolyte Interface of $Li(Ni_{0.8}Co_{0.1}Mn_{0.1})O_2$ on Electrochemical Performance during High Voltage Cycling Process. *J. Energy Chem.* **2020**, *47*, 72-78.

(60) Cherkashinin, G.; Nikolowski, K.; Ehrenberg, H.; Jacke, S.; Dimesso, L.; Jaegermann, W. The Stability of the SEI Layer, Surface Composition and the Oxidation State of Transition Metals at the Electrolyte-Cathode Interface Impacted by the Electrochemical Cycling: X-Ray Photoelectron Spectroscopy Investigation. *Phys. Chem. Chem. Phys.* **2012**, *14* (35), 12321.

(61) Zhang, J.-N.; Li, Q.; Wang, Y.; Zheng, J.; Yu, X.; Li, H. Dynamic Evolution of Cathode Electrolyte Interphase (CEI) on High Voltage $LiCoO_2$ Cathode and Its Interaction with Li Anode. *Energy Storage Mater.* **2018**, *14*, 1-7.

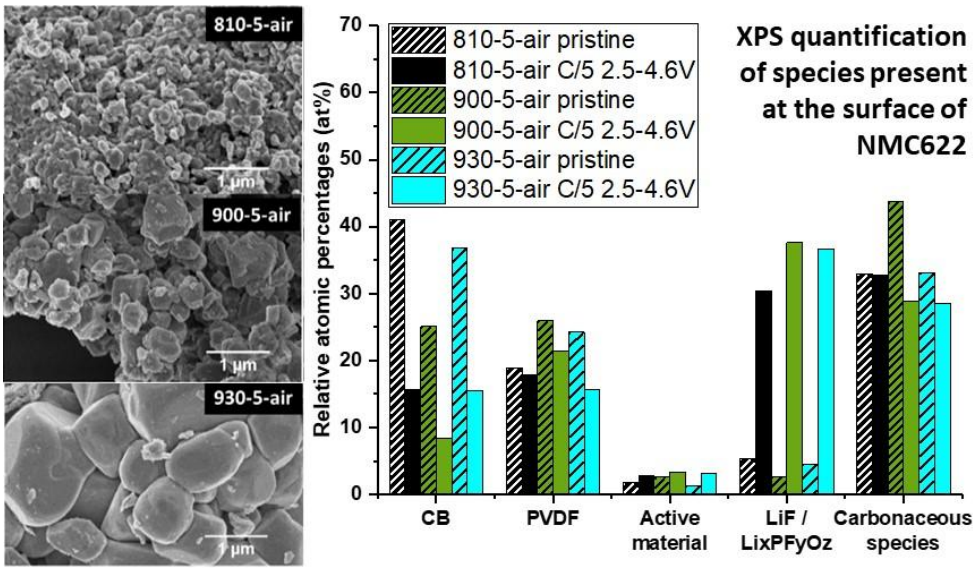

For Table of Contents only